Contrib Mineral Petrol (2017) 172:39
DOI 10.1007/s00410-017-1353-1

ORIGINAL PAPER

Competing effects of crystal chemistry and silicate melt composition on trace element behavior in magmatic systems: insights from crystal/silicate melt partitioning of the REE, HFSE, Sn, In, Ga, Ba, Pt and Rh

L. T. Michely[1] · F. P. Leitzke[1] · I. M. Speelmanns[1,2] · R. O. C. Fonseca[1]

Received: 8 September 2016 / Accepted: 29 March 2017 / Published online: 23 May 2017

Abstract We present new partition coefficients for the REE, HFSE, Sn, In, Ga, Ba, Pt and Rh between clinopyroxene, olivine and basaltic melt as a function of crystal chemistry and melt composition at temperatures of 1190–1300 °C and 1-bar pressure. Two components, namely Al_2O_3 and Na_2O, were chosen to be investigated since they are known to affect the structure of silicate melts and especially clinopyroxene crystal chemistry. The amount of $^{[4]}Al$ in clinopyroxene will result in an increase of $D_i^{cpx/melt}$ even after applying a correction factor to account for the effect of melt polymerization. Moreover, the positive correlation between $^{[4]}Al$ and $D_i^{cpx/melt}$ is not restricted to the REE, but also applies for Sn, Ga, In, and Ba. The addition of up to 2.6 wt% Na_2O to the silicate melt universally increases the $D_i^{cpx/melt}$ without any concomitant change in crystal chemistry or a significant effect in melt polymerization. This compositional effect is likely due to the ability of Na to break REE–Al complexes in the melt. Our results emphasize the importance of considering all variables that affect the behavior of trace elements in magmatic systems before applying the lattice strain model and derive meaningful results for the changes in the parameters of the crystallographic sites.

Keywords Trace elements · Experimental petrology · Partition coefficients · REE · HFSE

Communicated by Othmar Müntener.

Electronic supplementary material The online version of this article (doi:10.1007/s00410-017-1353-1) contains supplementary material, which is available to authorized users.

✉ L. T. Michely
LinaMichely@uni-bonn.de

[1] Steinmann-Institut für Geologie, Mineralogie und Paläontologie, Rheinische Friedrich-Wilhelms-Universität Bonn, 53115 Bonn, Germany

[2] Present Address: Institut für Geochemie und Petrologie, Eidgenössische Technische Hochschule (ETH) Zürich, 8092 Zurich, Switzerland

Introduction

The behavior of trace elements in magmatic systems is controlled by physico-chemical conditions prevalent during mantle partial melting and magmatic differentiation. Among these controlling factors are temperature, depth, type and degree of melting, source mineralogical composition and fO_2 (Onuma et al. 1968; Blundy and Wood 1994, 2003; Lundstrom et al. 1994; Wood and Blundy 1997; Westrenen et al. 2001; Evans et al. 2008). Different experimental approaches exist to investigate trace element partitioning between crystals and coexisting melt. One approach aims to produce trace element partitioning data under conditions that are directly applicable to a specific geological process or geodynamic setting. Although such experiments might yield the most appropriate crystal/silicate melt partition coefficients for trace elements and for specific geochemical process being modeled, they may easily become less relevant if conditions differ or if their values change dynamically throughout the process (see discussion in Westrenen et al. 2001). Another approach is to derive partition coefficients that can be applied to a wide range of dynamic settings. In this context, experiments are conducted in simple low-variance systems (i.e., only one variable is changed at a time), with the intent to assess their individual effects on trace element partitioning behavior. In order to generate a coherent, systematic dataset of crystal/silicate melt partition coefficients

for trace elements as a function of crystal composition, it is relatively straightforward to modify the bulk starting composition in order to achieve the desired change in crystal chemistry. However, it is often overlooked that it is challenging, if not impossible, to change crystal chemistry without changing melt composition, especially for phases that exhibit solid solutions, such as pyroxene and plagioclase. Because of this, it is often difficult to distinguish between the crystal chemistry and silicate melt compositional effects on trace element partitioning (e.g., O'Neill and Eggins 2002).

The degree of melt polymerization and melt structure is often described by employing common melt descriptors such as NBO/T (number of non-bridging oxygens per tetrahedrally coordinated cations) and the optical basicity parameter (OB) (e.g., Mills 1998; Moretti 2005). These parameters are well known to influence trace element partitioning (e.g., Gaetani 2004). However, melt compositional effects not accounted by NBO/T or OB have also been found in recent studies. For example, Evans et al. (2008) and Mallmann and O'Neill (2013) have shown that the partitioning of Sc, Y and the REE between olivine and silicate melt changes as a function of the mole fraction of $SiO_{2(melt)}$, rather than with NBO/T or OB. In the same sense, O'Neill and Eggins (2002) and O'Neill et al. (2008) suggested that CaO builds stable complexes with molybdenum and tungsten oxides in the melt. These stable complexes are presumably responsible for changes in the activity coefficient of these trace elements in the silicate melt (O'Neill and Eggins 2002) and affect the way they substitute in the crystals alongside the stoichiometric control.

The aim of this study is to identify the stoichiometric controls and melt compositional effects on the behavior of trace elements partitioning between clinopyroxene (cpx), olivine (olv), and silicate melt. We chose two chemical compounds, Al_2O_3 and Na_2O, since both are known to play a significant role in changing the structure of silicate melts and clinopyroxene crystal chemistry (cf. Lundstrom et al. 1994; Gaetani and Grove 1995; Hill et al. 2000). We present new crystal/silicate melt partitioning data for the REE, HFSE, Ga, Ba, Pt, Rh, Sn, and In obtained from experiments performed in vertical tube furnaces with temperatures ranging from 1190 to 1300 °C. The amount of sodium in the silicate melt was varied in order to cover the estimated concentration in the Earth's mantle (2590 μg/g, O'Neill and Palme 1998), as well as the average found in mid-ocean ridge basalts (2.7 wt%, Jenner and O'Neill 2012; Gale et al. 2013). The Al_2O_3 content in the cpx was also modified to cover a wide range of values (cf. Hill et al. 2000; Mollo et al. 2013). This enabled to eliminate the effect of melt polymerization and structure and isolate the individual effect of $^{[4]}Al$ on the crystal/silicate melt partitioning of trace elements. Moreover, the addition of Na_2O in the silicate melt enabled to identify a melt compositional effect on $D_i^{crystal/melt}$, which is yet not fully understood.

Methods

Experimental materials and methods

Four starting compositions in the CaO–MgO–Al_2O_3–SiO_2 (CMAS) system were synthesized. These compositions (Table 1) were chosen such that cpx was always a liquidus phase, and displayed a large enough range of $^{[4]}Al$ contents. Three compositions (HS, HE and HB) were modeled closely after Hill et al. (2000). In addition, a fourth composition (W1) was adopted from Fonseca et al. (2014) with the aim of producing $^{[4]}Al$-poor cpx. For further investigations concerning the effect of Na_2O on trace element partitioning between cpx and melt, the W1 composition was modified by adding variable amounts of Na_2O (CMAS + xNa_2O, 0 wt% $\leq x \leq$ 3 wt%). The use of the previously well studied W1 composition as a basis composition allowed to minimize co-varying factors having an influence on the partitioning of trace elements between cpx and melt, as the cpx crystallized from this composition always contained a negligible amount of $^{[4]}Al$ and the coexisting melt is fairly depolymerized (NBO/T >1.1). A further advantage of the W1 composition is that in one-atmosphere experiments olivine and cpx can crystallize simultaneously. While a change in the sodium concentration of the starting mix may affect the crystal chemistry of cpx, the olivine crystal composition will remain constant (Evans et al. 2008). Thus, the presence of both phases can be used as a tool to assess crystal and melt compositional effects on $D_i^{crystal/melt}$.

High purity (>99.5 %) oxide powders (SiO_2, MgO, Al_2O_3, Fe_2O_3, Cr_2O_3 and TiO_2) were ground with $CaCO_3$ and Na_2CO_3 under acetone in an agate mortar for ca. 10 min. Starting powder mixes were subsequently dried, pressed

Table 1 Starting compositions of the powder mixtures in cg/g

	HS	HE	HB	Wl	Wl + xNa_2O
SiO_2	45.02	52.97	43.18	47.79	48.21
$A1_2O_3$	17.11	16.13	17.41	5.12	5.17
MgO	12.45	13.12	12.1	25.75	26.03
CaO	25.06	17.43	27.12	17.91	18.04
Na_2O	0.36	0.35	0.19	–	x^a
Cr_2O_3	–	–	–	0.47	0.48
Fe_2O_3	–	–	–	0.49	0.50
P_2O_5	–	–	–	1	0.54
TiO_2	–	–		1	1.02
Total	99.66	99.64	99.86	99.53	100.0

[a] Variable amount of Na_2O (0 wt%> x <3 wt%)

into pellets and placed in a corundum crucible inside a vertical tube furnace to decarbonate overnight in air at 1 bar/950 °C. All pressed pellets were then re-ground under acetone and trace elements (Sc, Ni, Ga, Ge, Sn, In, Mn, Zr, Nb, Hf, Ta, Sm, Eu, Lu, La, Y, Th, and U) were added to the powders, in amounts of 500–1000 μg/g, as oxide powders or Specpure plasma standard solutions of 1000 μg/mL in 5% HNO_3. Barium was added as $BaCO_3$. The broad range of trace elements doped, especially to the W1 + x Na_2O, aimed at having enough cations to define the lattice strain parabolas by increasing the number of data points fitted to the lattice strain function (Blundy and Wood 1994).

A summary of the experimental run conditions is given in Table 2. Starting compositions were mixed with polyethylene glycol and water into a slurry, which was then placed in a Pt–Rh wire loop. The loops were suspended from a sample holder and loaded into the hotspot of a vertical tube gas-mixing furnace. The top and bottom of the furnace were kept open to maintain log fO_2 at −0.7 (equivalent to air), where the valence of trace elements is constant and no significant loss of Na is expected. Experiments were kept for 3–5 h at supraliquidus temperatures (1400 °C) to ensure complete melting of the powders and chemical homogenization prior to crystallization. The temperature during the experiments was monitored by an internal type B ($Pt_{94}Rh_6$–$Pt_{70}Rh_{30}$) thermocouple and was initially calibrated against the melting point of gold (cf. Laurenz et al., 2010, 2013), and found to be within 5 °C of it. Cooling ramps were around 0.05 °C/min to ensure adequate crystal growth (at least 100 μm) for LA-ICP-MS analysis. After reaching the target temperature, samples remained 48–86 h in the furnace to establish equilibrium between the crystals and the coexisting melt. Subsequently, experiments were quenched in air by removing the holder from the top of the furnace, which has a water-cooling system that keeps the temperature constant at 25 °C. Loops were then mounted in epoxy resin and its surface was polished for chemical analysis.

Analytical techniques

Concentration of major and minor elements (CaO, SiO_2, MgO, Al_2O_3, Na_2O, Fe_2O_3, Cr_2O_3 and TiO_2) in the crystals and silicate melt were acquired with a JEOL JXA-8200 electron microprobe. Analysis were carried out using wavelength dispersive mode (WDS) employing an accelerating voltage of 15 kV and 15 nA beam current, with an electron beam defocused to 5 μm. Most of the of major element oxides were calibrated on a natural basalt from the Juan de Fuca ridge (VG2, Jarosewich et al. 1980, while Na_2O was calibrated using a jadeite-diopside eutectic glass and TiO_2 in rutile, employing peak to background calibrations and the ZAF correction algorithm to account for the different electron absorption properties of our samples and the standards used. Major element concentrations are given as an average of 5–10 representative spots on each phase.

Trace element abundances were acquired with a Resonetics Resolution M50-E 193 nm Excimer laser ablation apparatus coupled to a Thermo Scientific XSeries II Q-ICP-MS at the Steinmann Institute, University of Bonn. The nuclides ^{29}Si, ^{43}Ca, ^{45}Sc, ^{55}Mn, ^{60}Ni, ^{69}Ga, ^{71}Ga, ^{72}Ge, ^{74}Ge, ^{89}Y, ^{90}Zr, ^{91}Zr, ^{93}Nb, ^{103}Rh, ^{115}In, ^{118}Sn, ^{120}Sn, ^{121}Sb, ^{123}Sb, ^{137}Ba, ^{138}Ba, ^{139}La, ^{151}Eu, ^{153}Eu, ^{152}Sm, ^{154}Sm, ^{175}Lu, ^{177}Hf, ^{178}Hf, ^{181}Ta, ^{182}W, ^{184}W, ^{195}Pt, ^{232}Th and ^{238}U were monitored during LA-ICP-MS analysis. The spot size was set between 44 and 73 μm to avoid melt inclusions, which are ubiquitous in experimental work (see e.g., Fonseca et al. 2014). For a secure melt-free analysis of the crystals, barium was used as a reference, because it is highly incompatible in cpx and olivine (cf.Lundstrom et al. 1994; Mollo et al. 2013). On each sample, five spot analyses in the glass and at least ten spots in the crystals were carried out using a laser fluency of ~6 J/cm^2 and a repetition rate of 15 Hz. For each measured spot, 15 s of background signal were followed by 30 s of ablation signal. The NIST-SRM-612 glass (Jochum et al. 2011) was used as the external standard, with measurements carried out via

Table 2 Experimental run conditions and products

Experiment	Cooling ramp (°C/min)[a]	Temp. (°C)	Run time (h)[b]	Eq. phases
HS1	0.1–1270; 0.05–1220	1220	3 + 74	cpx+glass
HE1	0.1–1280; 0.05–1190	1190	3 + 86	cpx+glass
HE2	0.1–1280; 0.05–1240	1240	3 + 70	cpx+glass
HB1	0.1	1270	3 + 48	cpx+an+glass
Wl	0.05	1300	3 + 56	cpx+ol+glass
Wl + x Na_2O	0.05	1288	4 + 72	cpx-ol+glass[c]

[a] In the case of two-step cooling ramp, the first step was performed on supraliquidus temperature and the second step during crystal growth

[b] Time experiment spent above supraliquidus (50–100 °C above target T.) + the time spend to equilibrate after cooling

[c] Experiments did not always crystallize both phases

standard/sample bracketing with no more than ten samples measured between each standard measurement. Additional spots were carried out in the NIST-610 glass, which was treated as an unknown to check for data accuracy. Obtained concentrations on the NIST-610 were found to be within 5–10 % within the reported values (Jochum et al. 2011). To correct for differences in ablation efficiency count rates were normalized either by ^{29}Si or ^{43}Ca, which were used as internal standards for olivine, clinopyroxene and melt, respectively. Data reduction was carried out employing the methodology described by Longerich et al. (1996).

Experimental results

Major, minor and trace element compositions of each crystalline and melt phase were found to be widely homogeneous (Table 3 and Supplementary Material), indicating a close approach to chemical equilibrium during the experiments. Although several trace elements were doped to the experiments, their combined abundance did not add up to more than 2 wt%, and as such, Henry's law was likely obeyed (cf. Gaetani 2004). Calculated partition coefficients are depicted in Table 4. A major concern when dealing with volatile elements (e.g., Sn, Sb, Ge and In) is their loss during the experimental run (e.g., Mallmann et al. 2014). Trace element concentrations of Sn, Sb and Ge in our experiments show a significant depletion from the initially doped amount, with final concentrations generally below 10 μg/g in the silicate glass. Indium loss was also found in the experimental runs, albeit relatively minor with a final concentrations of several hundreds of μg/g. Gallium is refractory under the experimental conditions of our study, and the measured Ga concentrations do not show a depletion relative to the amount that was initially doped.

CMAS system

All experiments carried out in the CMAS system crystallized euhedral to subhedral homogeneous clinopyroxene in equilibrium with silicate glass. In one single case (HB1), clinopyroxene crystals were found inter-grown with anorthite. The silicate glass, as well as the crystal compositions, display a broad range of SiO_2 and Al_2O_3 concentration, while smaller variations are observed for CaO and MgO. The tetrahedrally coordinated Al in cpx ($^{[4]}$Al) ranges between 0 and 0.27 apfu (Table 3). The broad range of $^{[4]}$Al contents in cpx allows us to study its effect on $D_i^{\text{cpx/melt}}$ in a systematic fashion. Unfortunately, it was not possible to vary the $^{[4]}$Al in cpx without changing melt composition, i.e., changes in the degree of melt polymerization were unavoidable, with NBO/T ranging from 0.5 to 1.1 (Table 3).

Crystal/silicate-melt partition coefficients as a function of the $^{[4]}$Al content in clinopyroxene

The REE and Y show a clear positive correlation with increasing $^{[4]}$Al content in cpx for all experiments. However, for two compositions, HE1 and HE2, with $^{[4]}$Al of 0.115 and 0.048, respectively, the $D_{REE+Y}^{\text{cpx/melt}}$ are higher than the overall trend of $D_{REE+Y}^{\text{cpx/melt}}$ versus $^{[4]}$Al (Fig. 1). Barium is more compatible in cpx as a function of $^{[4]}$Al (Fig. 1h). Crystal/silicate melt partitioning of Sn and In as a function of $^{[4]}$Al are scarce in the literature (e.g., Hill et al. 2000; Adam and Green 2006) and our new partitioning data can be used to better constrain a positive correlation between their $D_{Sn,In}^{\text{cpx/melt}}$ and $^{[4]}$Al in the cpx. Even considering that our experiments were prone to volatile loss, the agreement between our data and that reported by Hill et al. (2000), who performed experiments with sealed capsules, suggests that equilibrium was reached in our experiments.

CMAS + $x\mathbf{Na_2O}$ system

The second experimental series yielded fosterite and clinopyroxene crystals. Clinopyroxene crystals reached up to a mm in size, while fosterite crystals remained distinctly smaller (<50 μm). In some experiments olivine crystals were too small to be analyzed using LA-ICP-MS so the olivine dataset is not as extensive as for cpx. The cpx composition shows a dependence on the amount of sodium added to the starting composition (Table 3). However, even though the Na_2O content of the cpx varies proportionally with the Na_2O content of the melt, it remains consistently small (0.002–0.02 Na apfu). The $^{[4]}$Al in cpx in this series was designedly low (0.02–0.045 Al apfu) and melt composition shows small variations between the experiments depending on the initial amount of Na_2O (0.05–2.61 wt%), the degree of crystallization and whether cpx and olivine co-exist. Accordingly, NBO/T (1.1–1.3) and OB (0.6) variation is negligible when compared to the first experimental series (compare Table 3).

Crystal/silicate-melt partitioning as a function of $Na_2O_{(melt)}$

Regarding divalent cations, $D_{Ba}^{cpx/melt}$ and $D_{Pt}^{\text{cpx/melt}}$ correlate positively with $Na_2O_{(melt)}$ (Fig. 2a, b), while $D_{Ni}^{\text{cpx/melt}}$ (Fig. 2c) and $D_{Mn}^{\text{cpx/melt}}$ tend to be broadly insensitive to this parameter. Platinum may be tetravalent under very oxidizing conditions, such as with a pure O_2 atmosphere (Ertel et al. 1999). However, the proportion of Pt^{4+} over most of the range of fO_2 studied was deemed negligible (cf. Ertel et al. 1999), so it is very likely the Pt^{2+} is the oxidation state of Pt in our experiments. Crystal/silicate melt

Table 3 Major oxide composition cg/g of crystalline phases and silicate glass

Exp.	Temp (°C)	Phase	SiO_2	MgO	CaO	Al_2O_3	Na_2O	FeO	TiO_2	Cr_2O_3	T.E.	Total	Total Al (apfu)	$^{[41]}$Al (apfu)	Na (apfu)	NBO/T[a]
Experiments in the CMAS system																
HS1	1220	Melt	47.60 (48)	6.32 (4)	25.70 (11)	19.89 (18)	0.32 (4)				0.60	100.43				0.72
		cpx	48.39 (63)	13.55 (27)	25.55 (21)	13.47 (63)	0.04 (2)				0.44	101.44	0.57	0.27		
HE1	1190	Melt	55.9 (21)	7.79 (13)	16.72 (6)	18.49 (15)	0.38 (6)				0.44	99.72				0.50
		cpx	52.98 (18)	17.70 (19)	23.44 (25)	6.68 (20)	0.05 (2)				0.23	101.08	0.28	0.12		
HE2	1240	Melt	59.24 (34)	8.55 (16)	15.11 (15)	15.92 (15)	0.67 (2)				0.79	100.28				0.53
		cpx	54.99 (29)	18.99 (27)	22.97 (14)	3.95 (34)	0.052 (2)				0.40	101.35	0.17	0.05		
HB1	1240	Melt	46.72 (75)	8.34 (31)	29.31 (92)	16.47 (101)	0.21 (2)				0.78	101.83				1.04
		cpx	50.53 (50)	14.89 (32)	25.27 (33)	9.78 (83)	0.02 (1)				0.27	100.76	0.41	0.19		
W1	1300	Melt	54.64 (24)	15.62 (12)	16.73 (7)	8.91 (9)	0.105 (3)	0.72 (5)	1.78 (1)	0.02 (1)	0.86	99.20				1.10
		cpx	56.56 (14)	21.90 (25)	20.88 (34)	0.85 (6)		0.24 (5)	0.36 (4)	0.04 (1)	0.13	100.96	0.04			
		Olivine	44.02 (14)	55.59 (63)	0.47 (4)	0.016 (10)	0.12 (9)	0.17 (2)				100.39	0.001			
Experiments in the CMAS + $x$$Na_2O$-system																
W1-1	1286	Melt	53.05 (34)	15.22 (4)	20.57 (9)	6.55 (12)	1.12 (7)	0.74 (10)	1.35 (9)	0.016 (5)	1.36	99.98				1.4
		Olivine	43.07 (42)	55.82 (21)	0.58 (3)	0.026 (16)	0.023 (3)	0.19 (7)			0.57	100.28	0.001			
W1-2	1286	Melt	52.66 (19)	16.08 (7)	18.36 (12)	8.57 (11)	0.049 (32)	0.73 (9)	1.58 (7)	0.02 (1)	1.83	99.88				1.2
		cpx	55.61 (20)	21.35 (52)	21.82 (45)	0.82 (13)	0.03 (1)	0.18 (3)	0.31 (12)	0.05 (3)	0.30	100.47	0.03	0.02	0.002	
		Olivine	42.67 (70)	55.54 (35)	0.53 (3)	0.038 (17)	0.017 (13)	0.16 (3)	0.022 (8)		0.65	99.63	0.001			
W1-3	1286	Melt	51.65 (18)	13.85 (9)	17.27 (7)	10.35 (7)	1.73 (9)	0.70 (6)	2.23 (9)	0.022 (16)	2.17	99.97				1.1
		cpx	55.14 (47)	20.00 (24)	23.11 (48)	1.26 (22)	0.19 (4)	0.27 (6)	0.51 (9)	0.021 (14)	0.38	100.88	0.05	0.03	0.13	
		Olivine	42.67 (69)	55.52 (21)	0.63 (2)	0.02 (1)	0.017 (1)	0.18 (5)		0.011 (8)		99.05	0.001			
W1-4	1286	Melt	52.14 (3)	13.69 (9)	17.03 (12)	9.81 (18)	2.61 (10)	0.84 (3)	1.83 (6)	0.022 (12)	2.06	100.03				1.1
		cpx	54.91 (48)	19.33 (18)	23.55 (29)	1.30 (22)	0.28 (4)	0.30 (3)	0.60 (16)	0.009 (2)	0.47	100.75	0.06	0.03	0.02	
		Olivine	42.17 (63)	55.48 (10)	0.71 (2)	0.04 (1)	0.024 (19)	0.15 (5)	0.03 (2)	0.014 (13)		98.62	0.001			
W1-5	1286	Melt	52.56 (14)	13.62 (11)	16.74 (9)	9.73 (9)	2.43 (6)	1.04 (5)	1.79 (8)	0.013 (12)	2.09	100.01				1.1
		cpx	54.34 (63)	19.5 (1)	23.35 (9)	1.33 (4)	0.27 (3)	0.33 (6)	0.49 (4)	0.006 (6)	0.48	100.10	0.06	0.05	0.02	
		Olivine	42.89 (55)	55.49 (21)	0.66 (2)	0.04 (1)	0.029 (26)	0.15 (6)	0.018 (14)	0.011 (8)		99.29	0.001			
W1-6	1286	Melt	53.09 (46)	15.00 (8)	20.32 (12)	6.56 (7)	1.70 (9)	0.77 (3)	1.33 (5)	0.25 (20)	1.41	100.43				1.4
		Olivine	42.88 (34)	55.53 (45)	0.77(1)	0.03 (1)	0.04 (2)	0.15 (4)	0.028 (1)	0.014 (11)	0.47	99.91	0.001			

Values in parenthesis correspond to the one sigma standard deviation from the mean value, and correspond to its last significant digits

[a]NBO/T: number of non-bridging oxygens per tetrahedrally coordinated cations; OB: optical basicity; calculated based on the methodology of Mills (1998). T.E.: total of trace elements (LA-ICP-MS, Supplementary Table 1)

Table 4 Trace element crystal/silicate melt partition coefficients with one standard deviation of the mean value, given here as the last significant digits in parenthesis

cpx/melt	D_{Al}	σ	D_{Sc}	σ	D_{Cr}	σ	D_{Mn}	σ	D_{Ni}	σ	D_{Ga}	σ	D_{Y}	σ	D_{Zr}	σ	D_{Nb}	σ	D_{Rh}	σ	D_{In}	σ
HS1											0.731	(65)	0.642	(46)							2.26	(26)
HE1											0.454	(23)	0.747	(66)							1.42	(13)
HE2											0.317	(21)	0.591	(49)							1.38	(20)
HB1											0.572	(74)	0.424	(34)								
Wl											0.090	(8)	0.166	(12)								
Wl-2	0.096	(15)	0.80	(10)			0.484	(46)	1.371	(99)	0.0942	(11)	0.1591	(12)	0.0214	(60)	0.0012	(2)	2.86	(24)	0.327	(27)
Wl–3	0.122	(21)	1.65	(16)			0.387	(35)	1.439	(119	0.119	(14)	0.198	(22)	0.0475	(72)	0.0021	(2)	4.26	(73)	0.831	(53)
Wl–4	0.133	(22)	2.24	(14)			0.380	(26)	1.521	(78)	0.137	(6)	0.260	(35)	0.0893	(72)	0.0038	(6)	6.05	(144)	0.952	(44)
Wl–5	0.137	(4)	2.32	(16)			0.358	(19)	1.363	(75)	0.146	(7)	0.251	(17)	0.1089	(160)	0.0051	(17)	5.24	(54)	0.973	(54)

cpx/melt	D_{Sn}	σ	D_{Ba}	σ	D_{La}	σ	D_{Sm}	σ	D_{Eu}	σ	D_{Lu}	σ	D_{Hf}	σ	D_{Ta}	σ	D_{Pt}	σ	D_{Th}	σ	D_{U}	σ
HS1	12.8	(29)	0.00182	(84)	0.137	(20)	0.583	(42)	0.629	(35)	0.605	(31)					0.114	(48)				
HE1	2.83	(32)	0.00168	(88)	0.112	(14)	0.586	(77)	0.675	(86)	0.661	(70)					0.060	(5)				
HE2	3.6	(11)	0.00085	(25)	0.093	(11)	0.481	(46)	0.526	(41)	0.557	(78)					0.042	(15)				
HB1	5.9	(12)	0.00081	(24)	0.084	(14)	0.357	(53)	0.400	(60)	0.428	(70)					0.043	(15)				
Wl	0.48	(12)	0.00029	(23)	0.026	(4)	0.125	(11)	0.136	(11)	0.166	(13)					0.018	(5)				
Wl–2	0.19	(8)	0.00012	(1)	0.025	(4)	0.123	(12)	0.134	(12)	0.150	(14)	0.047	(14)	0.00111	(39)	0.023	(6)	0.0014	(4)	0.000070	(15)
Wl–3	0.46	(9)	0.00019	(2)	0.043	(2)	0.175	(18)	0.190	(20)	0.200	(19)	0.109	(16)	0.00283	(63)	0.045	(12)	0.0034	(3)	0.000203	(41)
Wl–4	0.40	(7)	0.00026	(4)	0.066	(17)	0.243	(33)	0.252	(34)	0.274	(36)	0.200	(13)	0.00608	(23)	0.089	(21)	0.0046	(9)	0.000177	(23)
Wl–5	0.67	(12)	0.00023	(4)	0.061	(6)	0.229	(16)	0.243	(18)	0.261	(18)	0.231	(30)	0.01072	(18)	0.106	(20)	0.0069	(16)	0.000208	(50)

Olivine/melt	D_{Al}	σ	D_{Sc}	σ	D_{Cr}	σ	D_{Mn}	σ	D_{Ni}	σ	D_{Ga}	σ	D_{Y}	σ	D_{Zr}	σ	D_{Nb}	σ	D_{Rh}	σ	D_{In}	σ
Wl-1	0.0040	(24)	0.099	(3)	0.97	(31)	0.820	(28)	10.5	(4)	0.0054	(9)	0.0044	(3)	0.00033	(5)			2.145	(362)	0.112	(6)
Wl–2	0.0044	(19)	0.092	(6)	0.67	(19)	0.678	(22)	8.8	(2)	0.0049	(5)	0.0029	(2)	0.00020	(3)			1.843	(146)	0.081	(3)
Wl–6	0.0046	(15)	0.119	(5)	1.36	(67)	0.847	(33)	10.2	(3)	0.0058	(7)	0.0062	(5)	0.00033	(1)			2.706	(325)	0.121	(8)

Olivine/melt	D_{Sn}	σ	D_{Ba}	σ	D_{La}	σ	D_{Sm}	σ	D_{Eu}	σ	D_{Lu}	σ	D_{Hf}	σ	D_{Ta}	σ	v_{Pt}	σ	D_{Th}	σ	D_{U}	σ
Wl-1			0.0000023	(8)	0.0000044	(18)	0.000212	(43)	0.000372	(19)	0.0177	(7)	0.00049	(9)	0.000025	(15)			0.0000012	(4)		
Wl–2			0.0000015	(11)	0.0000034	(9)	0.000142	(7)	0.000244	(17)	0.0122	(6)	0.00034	(2)	0.000008	(4)			0.0000017	(14)		
Wl–6			0.0000165	(77)	0.0000048	(16)	0.000365	(98)	0.000553	(65)	0.0245	(16)	0.00039	(8)	0.000046	(30)						

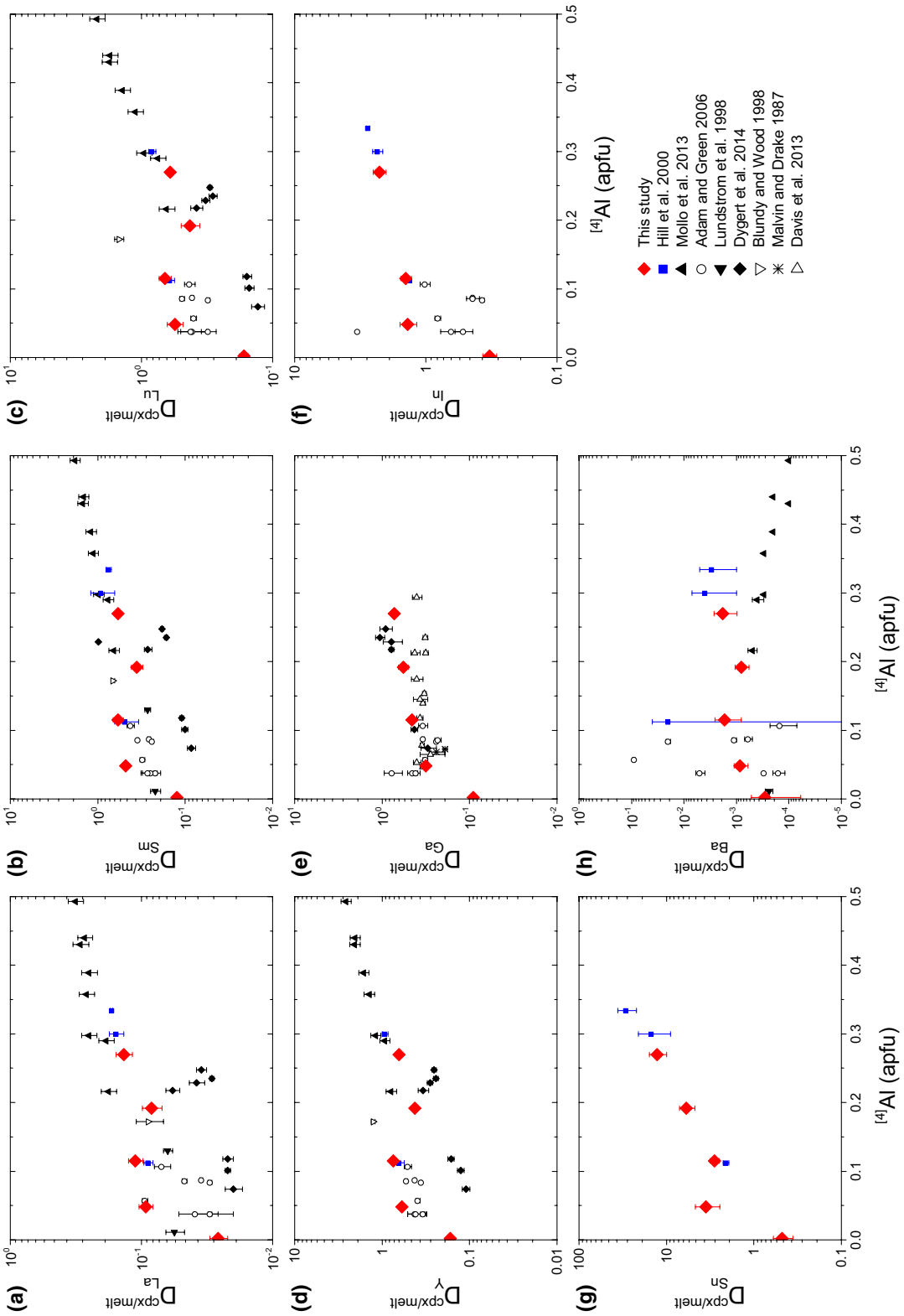

Fig. 1 Clinopyroxene/melt partition coefficient data plotted as a function of the tetrahedrally coordinated aluminum ($^{[4]}$Al). *Error bars* are one standard deviation. Literature data are taken from experiments ranging from 1050 to 1300 °C and pressures up to 3 GPa (Malvin and Drake 1987; Blundy et al. 1998; Lundstrom et al. 1998; Hill et al. 2000; Adam and Green 2006; Davis et al. 2013; Mollo et al. 2013; Dygert et al. 2014)

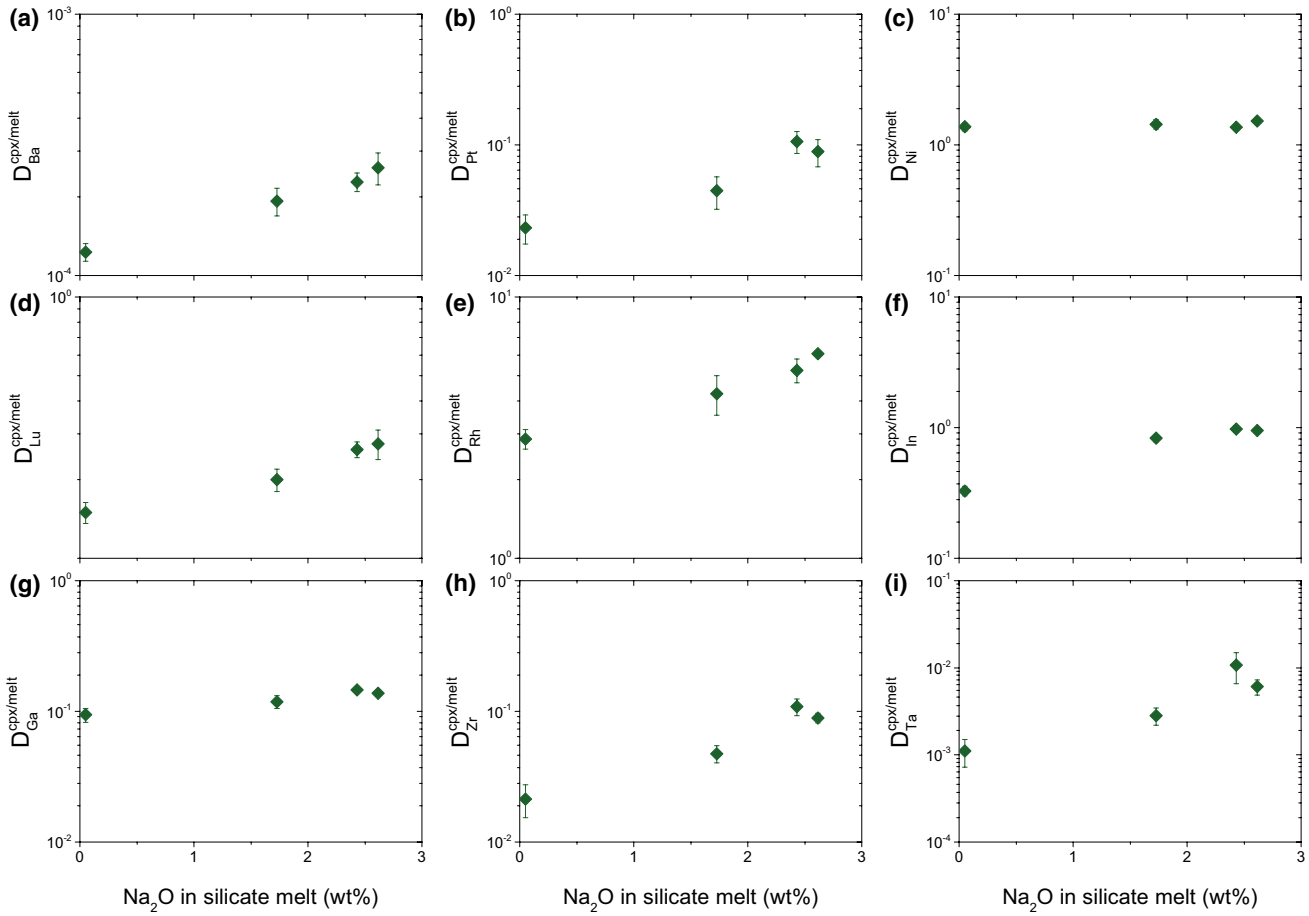

Fig. 2 Clinopyroxene/melt partition coefficient data plotted as a function of the Na_2O (wt%) content of the melt. *Error bars* are one standard deviation

partitioning of trivalent cations (REE, Y, Sc, Rh and In) show a linear positive increase with $Na_2O_{(melt)}$ (Fig. 2). The exception is Ga^{3+}, with $D^{cpx/melt}_{Ga}$ values being unaffected by the presence of Na_2O in the melt (Fig. 2g). The most surprising crystal/silicate melt partitioning behavior is observed for tetravalent and pentavalent cations (e.g., HFSE, Th, Sn, and Ge), with $D^{cpx/melt}_{i}$ values increasing by almost one order of magnitude with increasing $Na_2O_{(melt)}$ (e.g., Fig. 2i).

Evaluating olivine/silicate melt trace element partitioning data is challenging due to their low $D^{olivine/melt}_{i}$ values (e.g., Mallmann and O'Neill 2009; Fonseca et al. 2014). Therefore, analyses presented here have trace element concentrations in olivine which are at the detection limit or below. Despite this issue, it is possible to identify trends of $D^{olivine/melt}_{i}$ as a function of $Na_2O_{(melt)}$. Regarding divalent cations, $D^{olivine/melt}_{Ba}$ increases by around an order of magnitude over the range of $Na_2O_{(melt)}$ (Fig. 3a), while $D^{olivine/melt}_{Mn}$ (Fig. 3b) and $D^{olivine/melt}_{Ni}$ (Fig. 3c) remain constant. Olivine/melt partitioning of the trivalent REE, Y, and In show a distinct positive dependence on the amount of $Na_2O_{(melt)}$ (Fig. 3d–f). Gallium and Sc, although also trivalent at log $fO_2 = -0.7$, do not show a strong increase with $Na_2O_{(melt)}$. Chromium was not intentionally added to the starting compositions, but was present in most experiments as a contaminant (max. 5 μg/g), and $D^{olivine/melt}_{Cr}$ values increase with increasing $Na_2O_{(melt)}$, albeit within uncertainty. Values for $D^{olivine/melt}_{HFSE}$ (e.g., Fig. 3h,i) increase with $Na_2O_{(melt)}$, although with large associated errors due to their low concentration in the crystals (lower than 0.5 μg/g).

Discussion

Interplay between $^{[4]}$Al and melt compositional and structural effects on trace element partitioning

With the exception of Eu and Ce, the REE are homovalent elements that substitute into the M2 site of clinopyroxene in [8]-fold coordination (Gaetani and Grove 1995) and increase their $D^{cpx/melt}_{i}$ values with increasing $^{[4]}$Al

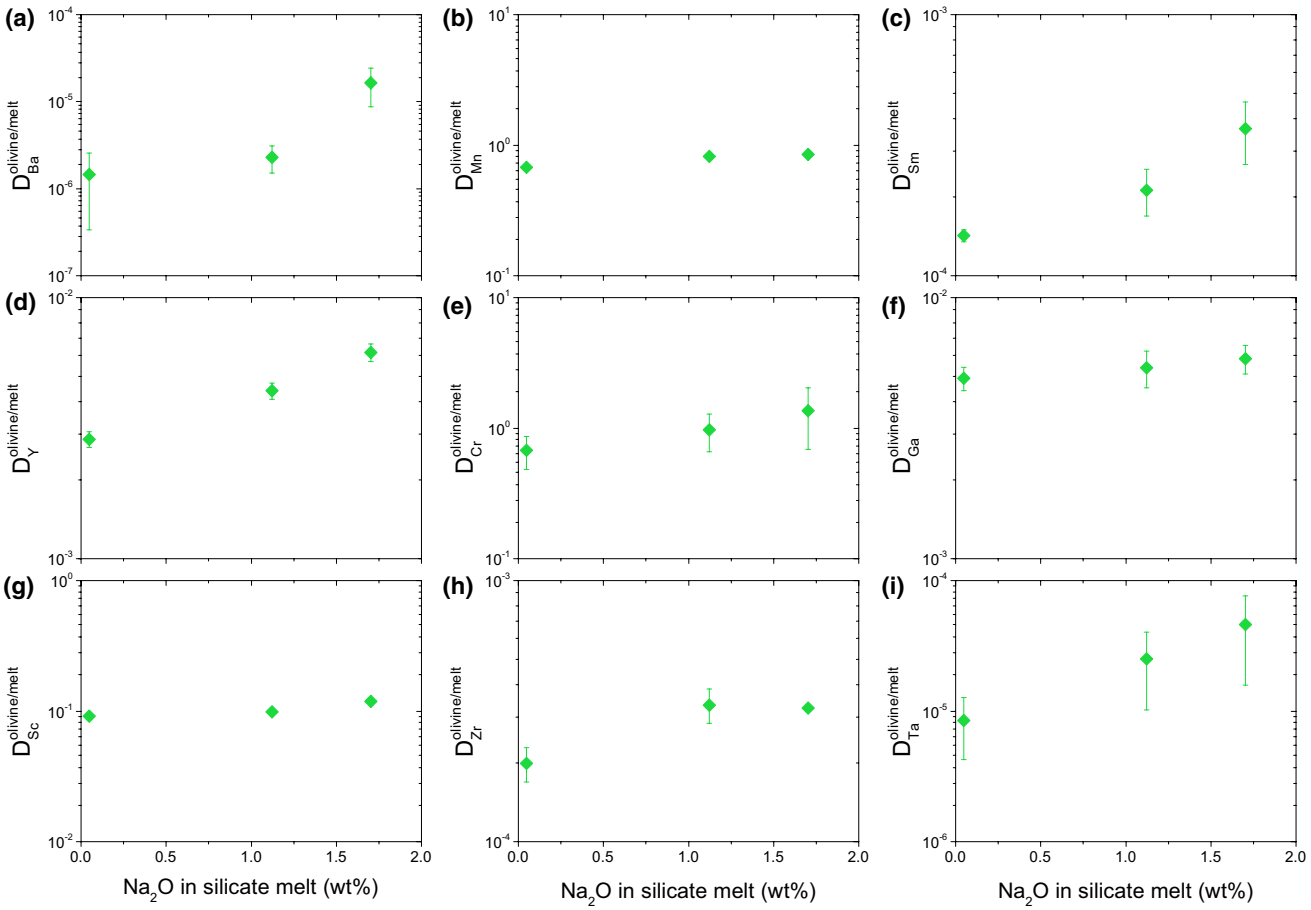

Fig. 3 Olivine/melt partition coefficient data plotted as a function of the Na_2O (wt%) content of the melt. *Error bars* are one standard deviation

content in cpx (e.g., Fig. 1a–d). However, our crystal/silicate melt partition coefficients obtained in two experiments (HE1 and HE2) are larger by one order of magnitude than the range of published experimental data with comparable $^{[4]}$Al in cpx (Fig. 1a–d; cf. Adam and Green 2006; Lundstrom et al. 1998). One likely explanation for this discrepancy is a change in the degree of melt polymerization given that the lowest NBO/T values reported in our study (ca. 0.5) were obtained for these two outlier experiments (HE1 and HE2). The degree of melt polymerization is not so easily decoupled from stoichiometric controls on crystal/silicate melt trace element partitioning (e.g., Ryerson and Hess 1978; Kohn and Schofield 1994; Blundy et al. 1998; Mysen 2004; Gaetani 2004; Huang et al. 2006). Several studies systematically observed the dependence of $D^{cpx/melt}_{\mathrm{REE}}$ on the degree of melt polymerization and have shown a distinct increase of partition coefficients of the REE with increasing melt polymerization (e.g., Gaetani 2004; Prowatke and Klemme 2005; Huang et al. 2006). Gaetani (2004), in particular, has shown that the influence of melt structure on $D^{\mathrm{cpx/melt}}_{REE}$ becomes significant for melt compositions with NBO/T values below 0.49, an expectation later confirmed by Huang et al. (2006).

Because it is almost impossible to change cpx crystal chemistry without changing melt composition (e.g., Mallmann and O'Neill 2009), it is necessary to find a way to isolate the individual effects of melt composition and structure from the addition of $^{[4]}$Al in the cpx on the $D_i^{\mathrm{cpx/melt}}$ values. To do this, we have used the experimental partitioning series for Mn and Zn between olivine and silicate melt as a function of NBO/T performed by Kohn and Schofield (1994). Because olivine composition remains the same over a range of NBO/T, one can assess the isolated effect of melt composition, which is best described by the following function:

$$\mathrm{D}_i^{\mathrm{olivine/melt}} = a * [\mathrm{NBO/T}]^b \quad (1)$$

The empirical approach of Kohn and Schofield (1994) can be extended to any cation that is exchanged between crystal and melt, provided of course, that a large enough dataset, covering a wide range of degrees of melt polymerization, exists. We used the experimental results of Gaetani (2004) and Huang et al. (2006), because their studies were set up

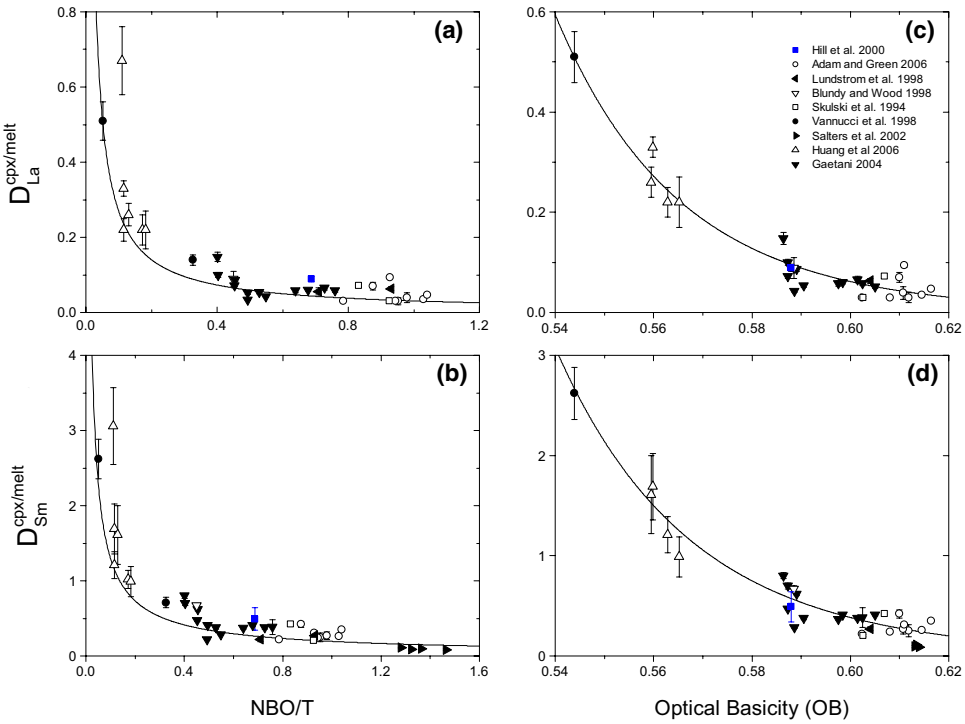

Fig. 4 $D_i^{cpx/melt}$ values of La (**a** + **c**) and Sm (**b** + **d**) are plotted as a function of NBO/T and OB, respectively. Only partitioning data for clinopyroxenes with similar crystal composition, used to minimize uncertainty, caused here by variable stoichiometry (e.g., variable $^{[4]}$Al). Partitioning data were fitted to an exponential function, the results of which are represented by the *full black lines* in the diagrams (see text for discussion). Similar regressions produced for crystal/silicate melt partitioning of Lu and Y can be found in the supplementary material

to systematically investigate the effect of melt structure on $D_{REE}^{cpx/melt}$, as well as additional data from the literature and plotted their partition coefficients vs. NBO/T (see Fig. 4). The largest dataset exists for La and Sm, while Eu partitioning data were found to be too few for a meaningful regression to be obtained. The scatter of the data obtained from different studies was found to be relatively large when compared to the goodness of the correlation obtained by Kohn and Schofield (1994), which is likely a result of the covariation of the clinopyroxene crystal composition with melt composition. Additionally, differences in the experimental conditions prevalent for each dataset, as well as data accuracy may be significant. Nevertheless, crystal/silicate melt partitioning data can be fitted reasonably well to Eq. (1) (e.g., Fig. 4a, b; Table 5).

The empirical fitting parameter a (Table 5) was found to vary according to the ionic radii of the elements and, hence, can be fitted to the lattice strain function (see Fig. 5), using the Levenberg–Marquardt iterative algorithm (Marquardt 1963). Because a is a cation-specific parameter and its value is dependent on the ionic radius of a given cation, the relation between $D_{REE+Y}^{cpx/melt}$ and ionic radius (r_i) , mimics that of the lattice strain function of Blundy and Wood (1994).

The exponent b (Table 5) does not show any systematic dependence on any of the specific properties (e.g., the ionic radius) of each element, and is not reflecting any physico-chemical change in the system. Therefore, it is likely that the differences in the values for

Table 5 Parameters obtained by fitting the partitioning data as a function of NBO/T according to the Eq. (1)

$D^{cpx/melt}$	a-factor	σ	b-exponent	σ	Adj. R^2
La	0.031	0.003	−0.94	0.13	0.36
Sm	0.194	0.021	−0.83	0.16	0.38
Y	0.353	0.024	−0.78	0.11	0.52
Lu	0.383	0.028	−1.06	0.14	0.68

Levenberg–Marquardt iterative algorithm was used for the fits (see text for details)

"b" exponents are due to variations in the experimental conditions (temperature and pressure), and starting composition from each experimental dataset. To be able to formulate a universal descriptor for the effect of NBO/T on the crystal/silicate melt partitioning of REE and Y, we can consider an average value of exponent b, which is essentially −1:

$$D_{REE+Y}^{cpx/melt} = a * [NBO/T]^{-1} \quad (2)$$

As such, Eq. 2 can be used to normalize crystal/silicate melt partition coefficients for REE and Y to the average NBO/T value of basaltic compositions (ca. 1—cf. Mysen 2004). This normalization (Table 6) is essential to separate the combined effects of melt polymerization and $^{[4]}$Al on the partitioning behavior of the REE and Y between clinopyroxene and silicate melt. The success

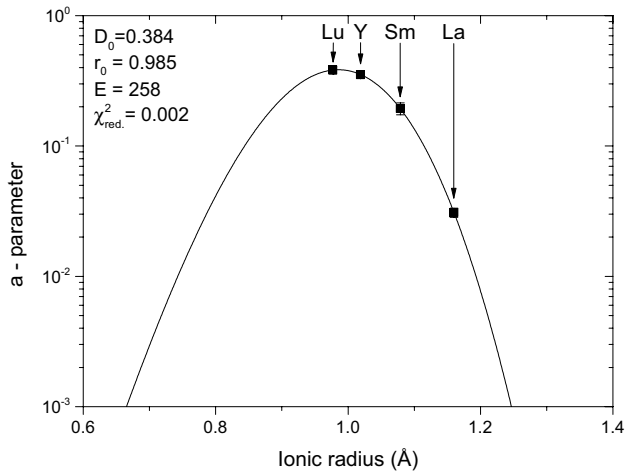

Fig. 5 The prefactor a plotted as a function of r_i regressed using the lattice strain function. If not visible, errors are smaller than symbol size

of this approach can be tested by assessing the agreement between our normalized $D_{REE+Y}^{cpx/melt}$ and the general trend obtained by Hill et al. (2000) as a function of $^{[4]}$Al (Fig. 6). Furthermore, we applied the same approach to normalize the $D_{REE+Y}^{cpx/melt}$ obtained by Mollo et al. (2013), which has NBO/T values around 0.5, and were able to achieve a similar good agreement (Fig. 6a, b).

However, the use of NBO/T has significant drawbacks, because it does not make a distinction between network modifiers like Ca or Mg (cf. Mills 1998). Some of these caveats can be partly addressed by using optical basicity (OB) as an alternative to NBO/T. The optical basicity of a silicate melt can be used in a similar way as NBO/T to describe its network (Mills 1998). The advantage of OB is that it takes the bond strength between cations and oxygens anions into account, i.e., their electronic polarizability and electronegativity (Duffy 1993; Mills 1998). Thus, OB differentiates between cations like Mg, Ca and Na that are essentially indistinguishable in the calculation of NBO/T. To evaluate a possible improvement of the correlation of $D_{REE}^{cpx/melt}$ with $^{[4]}$Al by normalizing the partition coefficients to the same OB in comparison to NBO/T, the same literature dataset of cpx/melt partition coefficients for the REE was used. The best fits of the literature partitioning data dependence on OB is through power functions as:

$$D_{La}^{cpx/melt} = 1(\pm 0.1) * 10^{-6} * [OB]^{-21.5(8)} \quad (3)$$

$$D_{Sm}^{cpx/melt} = 1.6(\pm 0.8) * 10^{-5} * [OB]^{-19.8(9)} \quad (4)$$

Table 6 Partition coefficient values normalized to NBO/T = 1 and OB = 0.61 applying correction factors (see text for details)

Experiment	OB	D_{Ba}	D_{La}	D_{sm}	D_{Eu}	D_Y	D_{Lu}	Norm. factor	D_{Ba}	σ	D_{La}	σ	D_{Sm}	σ	D_{Eu}	σ	D_Y	σ	D_{Lu}	σ
D normalized to an NBO/T of 1 yielding* *D*																				
HS1	0.72		0.137	0.583	0.629	0.642	5.605	1.34	0.0014	(6)	0.102	(17)	0.434	(52)1	0.469	(511	0.478	(57)	0.451	(48)
HE1	0.50		0.112	0.586	0.675	0.747	0.661	1.86	0.0009	(5)	0.06C	(9)	0.315	(461	0.362	(521	0.401	(45)	0.355	(44)
HE2	0.53		0.093	0.481	0.526	0.591	0.557	1.78	0.0005	(1)	0.052	(7)	0.271	(32)	0.296	(31)	0.332	(36)	0.314	(49)
HE (Hill et al. 2000)	0.69		0.117	0.581	0.737	0.783	0.689	1.40	0.0143	(140)	0.064	(8)	0.350	(12)	0.536	(65)	0.457	(70)	0.436	(53)
Experiment	OB	D_{Ba}	D_{La}	D_{sm}	D_{Eu}	D_Y	D_{Lu}	norm. factor	$'D_{Ba}$	σ	$'D_{La}$	σ	$'D_{Sm}$	σ	$'D_{Eu}$	σ	$'D_Y$	σ	$'D_{Lu}$	σ
D normalized to an OB of 0.61 yielding *'D*																				
HS1	0.609	0.0018	5.137	0.583	0.629	0.642	0.605	1.04	0.0018	181	0.132	1191	0.562	1411	0.61	131	0.62	151	0.58	131
HE1	0.579	0.0017	0.112	0.586	0.675	0.747	0.661	2.97	0.0006	(3)	0.038	(5)	0.197	(28)	0.23	(3)	0.25	(3)	0.22	(3)
HE2	0.573	0.0009	0.093	0.481	0.526	0.591	0.557	3.65	0.0002	(1)	0.025	(3)	0.132	(14)	0.14	(1)	0.16	(2)	0.15	(2)
W1	0.590	0.0003	0 076	0.125	0.136	0.166	0.166	198	0.00015	(11)	0.013	(2)	0.063	(6)	0.07	(1)	0.08	(1)	0.08	(1)
HB	0.622	0.0008	0.084	0.357	0.377	0.424	0.428	0.72	0.0011	(4)	0.117	(20)	0.499	(75)	0.53	(8)	0.59	(5)	0.60	(10)
HE (Hill et al. 2000)	0.618	0.020	0.117	0.581	0.737	0.783	0.689	0.77	0.0052	(39)	0.202	(25)	1.193	(37)	1.32	(3)	1.21	(9)	1.08	(7)
HS (Hill et al. 2000)	0.588	0.004	0.16	0.92	1.02	0.93	0.83	2.13	0.0094	(94)	0.042	(4)	0.230	(7)	0.35	(3)	0.30	(4)	0.29	(3)
HB (Hill et al. 2000)	0.622	0.003	0.169	0.750	0.770			0.67	0.0045	(30)	0.253	(7)	1.121	(77)	1.15	(37)				

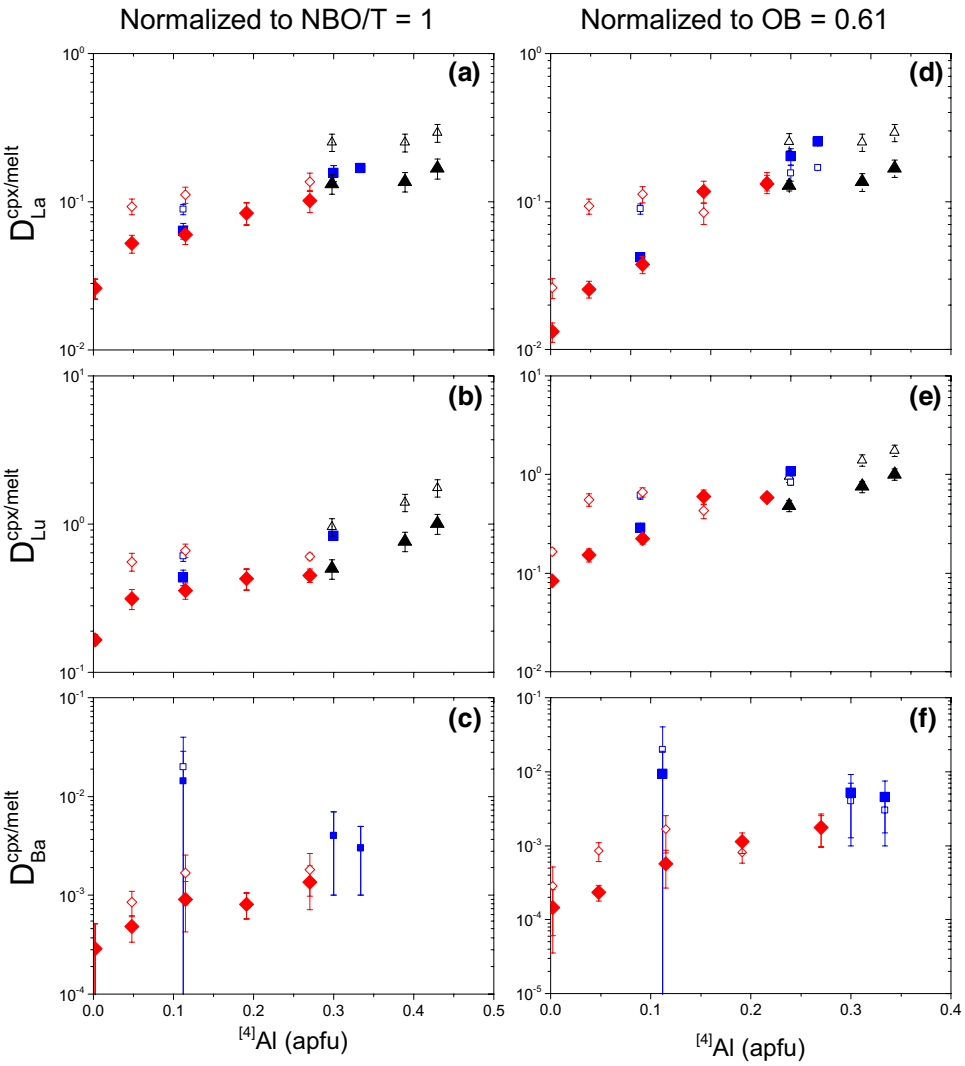

Fig. 6 Partition coefficients normalized to NBO/T = 1 (**a**–**c**) and OB = 0.61 (**d**–**f**) plotted as a function of the aluminum content in the tetrahedral position of cpx ($^{[4]}$Al). *Open symbols* are representative for the uncorrected (NBO/T≠1, OB≠0.61) partition coefficients, while filled symbols represent partition coefficients, which are normalized to either NBO/T = 1 or OB = 0.61 . **a**, **b** and **d**, **e** are representative for all REE and Y. **c** and **f** show how applying the same normalization factors determined for the REE (see Table 6) improves the correlation of $D_{Ba}^{cpx/melt}$ with $^{[4]}$Al. The *symbols* are consistent with those depicted in Fig. 1. *Error bars* are one standard deviation of the mean

The REE + Y partition coefficients were normalized to an OB value of 0.61 (Fig. 6d, e), which is close to the average expected for mid-ocean ridge basalts (Gale et al. 2013). Crystal/silicate melt partition coefficient values that were corrected from experiments with OB values ≥ 0.62 seem to be slightly offset from the overall correlation of $D_{REE+Y}^{cpx/melt}$ as a function of $^{[4]}$Al. The inefficiency of this procedure for OB values ≥0.62 might be the result of the lack of data used for the regressions in Fig. 4c, d. Nevertheless, OB seems to more accurately describe the melt compositional effect on $D_{REE+Y}^{cpx/melt}$ (Fig. 6), as it better distinguishes different chemical elements in the melt environment. Thus, normalizing the $D_{REE+Y}^{cpx/melt}$ values to the same OB more efficiently removes the melt compositional effect, isolating the crystal compositional effect of $^{[4]}$Al in cpx on crystal/silicate melt trace element partitioning.

Barium

Hill et al. (2000) assumed little or no change for 2+ cations substituting into the M2 site with increasing $^{[4]}$Al content of clinopyroxene, because the net charge of the site remains 2+, regardless of the amount of Al^{3+} in the cpx. Thus, it is reasonable to assume no change in the partitioning behavior for 2+ trace elements entering the M2 site. Indeed, divalent cations like Sr^{2+} display $D_{Sr}^{cpx/melt}$ that are near constant over a range of $^{[4]}$Al (Hill et al. 2000). However, our data show that $D_{Ba}^{cpx/melt}$ increases slightly with $^{[4]}$Al in clinopyroxene (Fig. 6), similarly to that observed for $D_{REE+Y}^{cpx/melt}$ (Fig. 6c, f). Huang et al. (2006) have shown that an increase in the degree of melt polymerization correlates positively with increasing $D_{Sr}^{cpx/melt}$ values. As Sr and Ba are both alkali earths, it seems reasonable to assume that the partitioning of

Ba between crystals and silicate melt is affected by melt polymerization similarly to Sr. As a consequence, $D_{Ba}^{cpx/melt}$ obtained for the HE1 and HE2 experiments in our study was also corrected to take into account the degree of polymerization (Table 6), and results show that corrected $D_{Ba}^{cpx/melt}$ values correlate positively with increasing $^{[4]}$Al.

Gallium

In similar fashion to the REE, $D_{Ga}^{cpx/melt}$ is shown here to correlate positively with the $^{[4]}$Al content in cpx (Fig. 1e), in agreement with the trend observed in literature data (Malvin and Drake 1987; Dygert et al. 2014). Based on our new $D_{Ga}^{cpx/melt}$ data, it remains unclear to what extent $D_{Ga}^{cpx/melt}$ depends on OB. In contrast to the REE + Y and Ba, Ga is a relatively small cation and it is assumed to have a structural role in silicate melts nearly identical to that of Hess (1991). Hence, one could assume that Ga^{3+} behaves as a network-forming, instead of a network-modifier cation and, thus, may contribute to increase melt polymerization (Mysen 1990). Nevertheless, inasmuch as our results are concerned, $D_{Ga}^{cpx/melt}$ is unaffected by an increase in the degree of melt polymerization.

The effect of $^{[4]}$Al on cpx M2 lattice site parameters based on normalized $D_{REE+Y}^{cpx/melt}$

After being able to filter the effect of melt polymerization from the dataset, we can re-evaluate how the addition of $^{[4]}$Al into the cpx T-site will influence the size and form of the octahedral neighboring sites. To do so, we fitted $D_{REE+Y}^{cpx/melt}$ normalized to the same optical basicity to the lattice strain function (Blundy and Wood 1994):

$$D_i^{crystal/melt} = D_0 \exp\left[\frac{-4\pi E N_A[\frac{r_0}{2}(r_i - r_0)^2 + \frac{1}{3}(r_i - r_0)^3]}{RT}\right], \quad (5)$$

where D_i is the partition coefficient of an element i and D_0 is the optimum, or strain-free partition coefficient that is reached when a fictive cation with an ideal ionic radius r_0 enters the crystal lattice site of interest and produces no elastic strain. The variable r_i represents the radius of a cation that enters the same site, but by doing so it produces variable elastic strain. The internal strain of a crystal site that result when $r_i \neq r_0$, is quantified by the apparent Young's modulus (E). N_A is the Avogadro's Number, R is the universal gas constant and T is absolute temperature (Blundy and Wood 1994).

In order to derive D_0, r_0 and E for trivalent elements entering the M2 site of cpx, the fitting was performed using the Levenberg–Marquardt iterative algorithm (for details see Marquardt 1963). From the fits, it is possible to observe an increase in $^{[4]}$Al coupled to a broad linear increase in the strain-free partition coefficient (D_0) (Fig. 7). Secondly, the optimum radius of the M2 crystal lattice site shifts to higher values, but the associated errors are relatively large, such that no clear trend can be deduced from the data. Young's elastic strain modulus (E) seems to be broadly constant, with exceptions for those experiments having a higher degree of melt polymerization. In a computer simulation of garnet-melt partitioning, Westrenen et al. (2000) studied a possible dependence of r_0 and E on the coexisting melt structure. Indeed, their results show that the absolute values of r_0 and apparent E depend on the adjacent melt environment, i.e., the coordination of trace elements in the melt (e.g., Ponader and Brown 1998; Prowatke and Klemme 2005; Westrenen et al. 2000). Although all variations of E

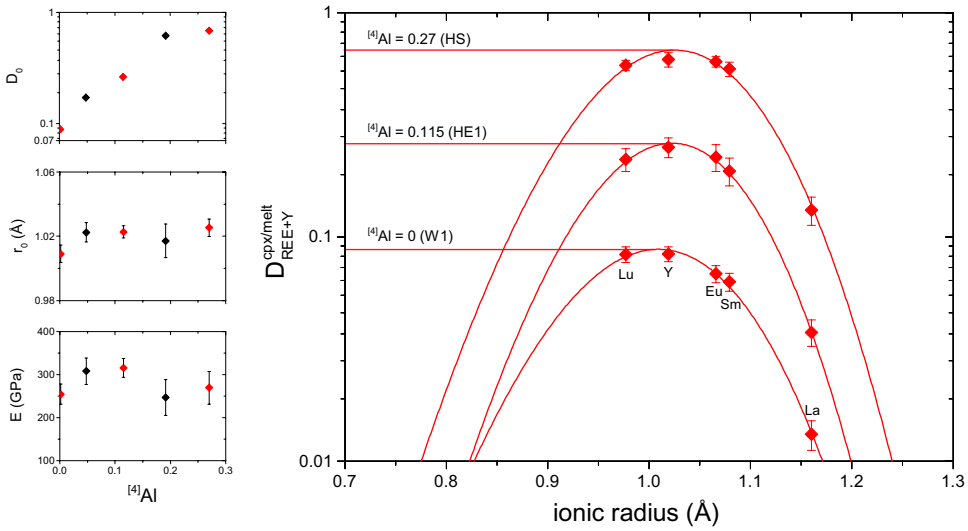

Fig. 7 Lattice strain model fits for a selection of experiments of this study at different $^{[4]}$Al contents based on REE partition coefficients normalized to an optical basicity of 0.61. Lattice strain parameters of all experiments are displayed as a function of the $^{[4]}$Al content of cpx and listed values of these parameters can be found in Table 7. The lattice strain parameters belonging to the depicted lattice strain parabolas in this figure are shown in *red*. *Error bars* are one standard deviation of the mean

in our study have a large degree of uncertainty, the overall pattern seems to support the assumption of Westrenen et al. (2000), i.e., that the lattice strain parameters E and r_0 are not only stoichiometrically controlled, but also depend on the melt environment.

The increase in $D_{Ba}^{cpx/melt}$ as a function of the $^{[4]}$Al content in cpx might be unrelated to the increase in the number of charge balancing configurations (Hill et al. 2000), but rather to changes in the internal strain E of the crystal lattice. The lattice strain parabola for 2+ cations in the M2 site (e.g., Ba) is assumed to flatten with increasing $^{[4]}$Al content in cpx (Lundstrom et al. 1998), which will lead to an increase of the partition coefficient of cations whose ionic radius places them on the outermost edges of the lattice strain parabola. Conversely, for cations whose r_i are closer to r_0, their respective $D_i^{crystal/melt}$ values should decrease as E and D_0 both decrease. However, given the limited amount of data for divalent elements in the M2 site available to produce a meaningful lattice strain fit, this possibility cannot be readily tested.

Interplay between Al_2O_3 and Na_2O in the silicate melt and its effect on the partitioning behavior of trace elements between crystals and silicate melt

Even though Na_2O plays an important role in the structure of silicate melts (e.g., Mills 1998), with contents as high as 5 wt% in mid-ocean ridge basalts (cf. Jenner and O'Neill 2012; Chemia et al. 2015), crystal/silicate melt partitioning studies are often performed in systems with little or no Na_2O (e.g., Gaetani and Grove 1995; Mallmann and O'Neill 2009). Clinopyroxene/silicate melt partitioning of Na is mainly controlled by the bulk Na_2O content of the system and pressure (Blundy et al. 1995; Flemming and Luth 2002), while the effect of temperature is assumed to be minor (Blundy et al. 1995). The crystal compositional effect on the partitioning of trace elements between cpx and silicate melt that arises due to the incorporation of sodium into the crystal lattice is most likely to be related to the increasing number of charge balancing configurations. However, previous experiments were not able to isolate the sole effect of the addition of sodium to a system on the partitioning behavior of trace elements (e.g., Bennett et al. 2004; Gaetani 2004). In this sense, we assess if the addition of sodium to the silicate melt exerts an influence on $D_i^{crystal/melt}$ of trace elements in a way that cannot be accounted by NBO/T or OB, such as by the formation of melt complexes (e.g., O'Neill and Eggins 2002; Dygert et al. 2013; Leitzke et al. 2016). Our experiments are designed to test this hypothesis, given that Na_2O bulk contents vary from 0 to 3 wt%, while the degree of melt polymerization and $^{[4]}$Al in cpx are constant (OB ca. 0.6 and $^{[4]}\text{Al} \leq 0.04$). Moreover, the composition of both cpx and olivine remained virtually unchanged. For example, the addition of 3 wt% Na_2O to the starting composition lead to only negligible variations in the sodium content of cpx, ranging between 0.013 and 0.02 Na apfu.

The effect of Na_2O in silicate melt on the partitioning behavior of trace elements has already been hinted upon previously. For example, Schosnig and Hoffer (1998), noted that additional Na_2O in the silicate melt caused an increase in crystal/silicate melt partition coefficients of the REE, which is decoupled from any change related to crystal chemistry. They found that in the experiments crystallizing high-Al diopside, $D_{REE}^{cpx/melt}$ values were twice as large in the presence of $Na_2O_{(melt)}$ relative to a Na-free silicate melt composition. The reason would be the formation of "REE^{3+}−Al−complexes", which are stable in the melt but have an offset to the ideal bonding length, bonding angle and the number of surrounding oxygen anions present, so that their incorporation into a growing diopside crystal is hampered (Schosnig and Hoffer 1998). When Na_2O is introduced into the system, these melt complexes may be modified or broken down to some extent, so that the compatibility of the REE into cpx increases. Within this framework, the increasing compatibility of the REE as a function of Na_2O_{melt} observed in our results could be explained by the formation of strong bonds between Na and Al in the silicate melt, which would break the "REE^{3+}-Al complexes" apart. The detachment of the REE from the aluminum in the silicate melt by the addition of Na_2O in the system will inevitably lead to an increase in the activity coefficients of their REE-O species and, consequently, to an increase of the crystal/melt partition coefficients (O'Neill and Eggins 2002).

Regarding crystal/silicate melt partitioning of divalent elements, $D_{Ba,Pt}^{crystal/melt}$ increase with increasing Na_2O_{melt}, while values $D_{Ni}^{crystal/melt}$ and $D_{Mn}^{crystal/melt}$ remain broadly constant. This can be explained by the significantly larger ionic radii in [6]-fold coordination of Ba^{2+} and Pt^{2+} when compared to Ni^{2+} and Mn^{2+} (VI coordination: Ba = 1.35 Å, Pt = 0.8 Å, Ni = 0.69 Å, Mn = 0.67 Å). Barium and Pt in [6]-fold coordination would have an ionic radius more similar to the REE than Mn and Ni, and, therefore, a greater affinity for being incorporated into the "REE^{3+}-Al complexes" in the melt. In addition to the disparity found for the behavior of divalent cations, the partitioning of trivalent and tetravalent cations between clinopyroxene, olivine, and silicate melt, are affected by Na_2O_{melt} to a different extent. The $D_{Ga,Ti,Al}^{crystal/melt}$ values increase significantly less as a function of Na_2O_{melt} (Fig. 8) when compared to the increase observed for $D_{REE,HFSE}^{crystal/melt}$ (Figs. 2, 3). This disparate behavior can be explained by the fact that Ga, Al and Ti are present in tetrahedral coordination in silicate melts (Hess 1991), and thus, occupy the same network-forming sites in the "REE^{3+}-Al complexes" in the melt.

The lattice strain model (Blundy and Wood 1994) can also be used to account for changes in melt composition. This is only possible if the partitioning behavior of all trace elements used to constrain the lattice strain parabola for that particular crystal site all show the same level of dependency on a given silicate melt component. This is the case for the cpx/silicate melt partitioning of REE and Y, which are equally affected by Na_2O_{melt} (Fig. 9). Therefore, we can use our $D_{REE+Y}^{cpx/melt}$ to fit the data to equation 5 and obtain the lattice strain parameters D_0, r_0 and E as a function of Na_2O_{melt}. Crystal/silicate melt partitioning data for In was not considered for the fits, as previous studies suggested that In partitions into both the M1 and M2 site of cpx (e.g., Hill et al. 2000). The lattice strain parameters r_0 and E remain constant over the increase in Na_2O_{melt}, while D_0 increases with the amount of Na_2O_{melt} (Table 7). Constant values of r_0 and E support the hypothesis that crystal composition is not the main control on the observed variation in $D_{REE+Y}^{cpx/melt}$ with Na_2O_{melt}. Compared to the number of

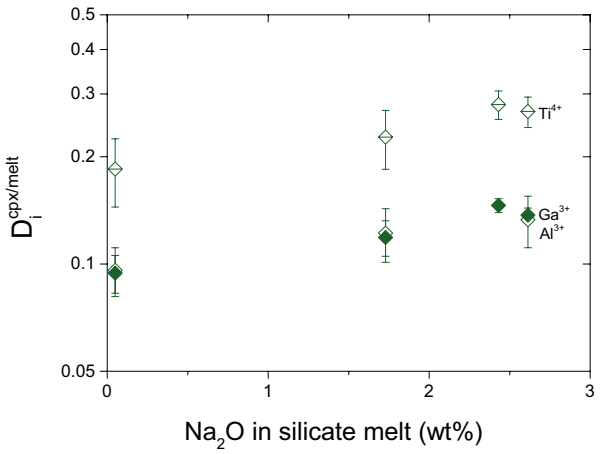

Fig. 8 Partitioning behavior of Al, Ga and Ti as a function of Na_2O_{melt}. The partitioning of Ga, Al and Ti between cpx and the silicate melt is affected in the exact same way by the amount of Na_2O_{melt}

Table 7 Summary of the lattice strain parameters obtained through fitting our partitioning data for homovalent elements to Eq. 5

Site	Valency	Comp.	Cations	X^2	D_0	σ	r_0	σ	E	σ
Clinopyroxene										
M2	3+	HS[a]	La, Sm, Eu, Lu, Y	0.493	0.682	(29)	1.025	(5)	270	(38)
M2	3+	HE1[a]	La, Sm, Eu, Lu, Y	0.139	0.262	(7)	1.023	(4)	316	(22)
M2	3+	HE2[a]	La, Sm, Eu, Lu, Y	0.295	0.171	(6)	1.022	(6)	308	(31)
M2	3+	HB[a]	La, Sm, Eu, Lu, Y	0.518	0.617	(25)	1.017	(10)	247	(42)
M2	3+	Wl[a]	La, Sm, Eu, Lu, Y	0.367	0.088	(2)	1.009	(5)	255	(24)
M2	3+	Wl-2	La, Sm, Eu, Lu, Y	0.261	0.165	(4)	1.016	(4)	277	(22)
M2	3+	Wl-3	La, Sm, Eu, Lu, Y	0.681	0.219	(10)	1.020	(8)	254	(31)
M2	3+	Wl-4	La, Sm, Eu, Lu, Y	0.608	0.288	(17)	1.018	(12)	217	(52)
M2	3+	Wl-5	La, Sm, Eu, Lu, Y	1.947	0.277	(15)	1.019	(11)	228	(45)
Ml	3+	HE1	Al[b], Cr[c], Sc[c]	1.64E-06	17.338[d]		0.666		1522	
Ml	3+	Wl-2	Al, Sc, Rh	8.07E-09	2.977		0.678		1238	
Ml	3+	Wl-3	Al, Sc, Rh	4.32E-07	4.426		0.678		1064	
Ml	3+	Wl-4	Al, Sc, Rh	1.89E-07	6.310		0.679		1128	
Ml	4+	Wl-2	Ti, Sn, Hf, Zr	0.045	0.535	(50)	0.648	(0)	3091	(192)
Ml	4+	Wl-3	Ti, Sn, Hf, Zr	0.217	1.114	(132)	0.654	(0)	3623	(228)
Ml	4+	Wl-5	Ti, Sn, Hf, Zr	0.007	1.288	(23)	0.657	(0)	3076	(33)
Ml	4+	Wl-3	Sn, Hf, Zr	0.344	1.211		0.648		3091	
Ml	4+	Wl-5	Sn, Hf, Zr	2.575	2.349		0.648		3091	
Olivine										
Ml/2	3+	Wl-1	Sm, Eu, Y, Lu, In	3.049	0.242	(13)	0.711		470	
Ml/2	3+	Wl-2	Sm, Eu, Y, Lu, In	0.998	0.182	(19)	0.711		470	
Ml/2	3+	Wl-6	Sm, Eu, Y, Lu, In	1.035	0.295	(18)	0.711		470	

[a] Partition coefficient of these experiments used to fit to the lattice strain function were normalized to the same OB of 0.61

[b] Partition coefficient of Al for the Ml site

[c] Partition coefficient values obtained by Hill et al. (2000) in an experiment with similar [4] Al content in cpx

[d] Error is not given if less then four data points were fitted to the lattice strain function, or if parameters were fixed to a specific value

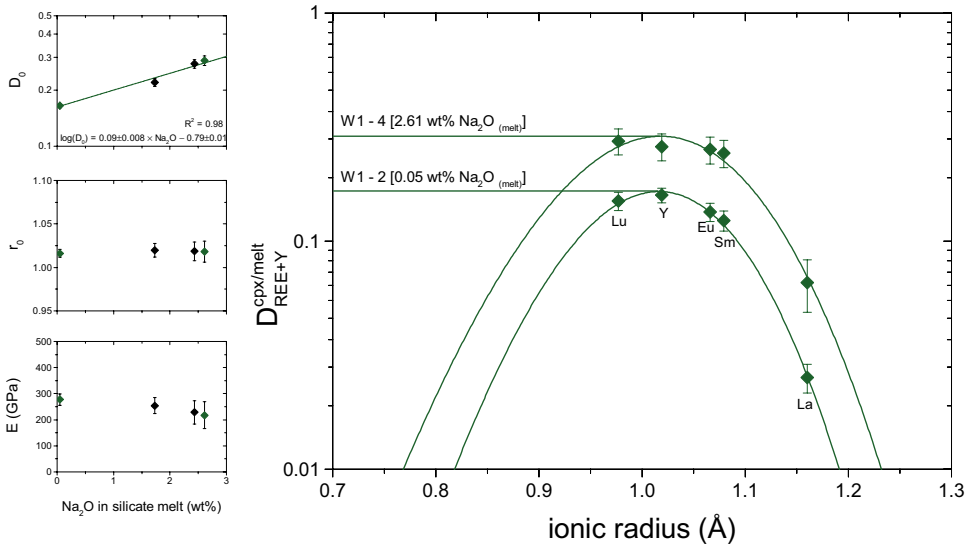

Fig. 9 Lattice strain model fits of the M2 site of cpx, based on the partitioning data of the REE and Y and displayed for a selection of different amounts $Na_2O_{(melt)}$. Lattice strain parameters of all experiments are displayed as a function of $Na_2O_{(melt)}$. Ionic radii in [8]-fold coordination were taken from Shannon (1976). The parameters belonging to the depicted lattice strain parabolas are *color coded*. The values of the lattice strain parameters D_0, r_0 and E are displayed in Table 7. *Error bars* are one standard deviation

trivalent trace elements substituting into the M2 site, there are only a few 3+ cations (Sc, Rh, Cr and Al) entering the M1 site of cpx in our experiments Hill et al. 2000, which limits the accuracy of the fits to Eq. 5. Nevertheless, it can be seen that E and r_0 for the M1 site of cpx change with Na_2O_{melt} (Table 7; Fig. 10), contrary to the observed for the M2 site of cpx (Fig. 9). The reason for the perceived variation in E is related to differences between how Al interacts with Na_2O in silicate melt when compared to Sc and Rh. In this case, the results of the lattice strain fit are not reflecting changes in the internal strain or distortion of the M1 site, but rather differences in the interaction parameters between the different trivalents substituting into the M1 site and Na_2O. As such, care should be taken in interpreting the results from lattice strain fits as in some cases they may not represent the actual strain of the mineral sites, but rather some complex interplay between melt and crystal compositional effects.

Clinopyroxene/silicate melt partitioning data for tetravalent cations entering the M1 site (e.g., Ti, Sn, Zr and Hf) was well reproduced using the lattice strain function, but only for the Na_2O-free experiment (Fig. 11). For the Na_2O -bearing experiments, $D_{Ti}^{cpx/melt}$ is not affected like the other tetravalent cations by changes in Na_2O in the silicate melt. We assume that Ti is mainly in five or sixfold coordination in basaltic magmas (Farges et al. 1996), and enters the octahedral site of clinopyroxene (e.g., Fonseca et al. 2014). The lattice strain parameters obtained when using Sn, Zr, Hf and Ti partitioning data (see dashed lines in Fig. 11) show that E and r_0 shift in order to account for the differences in partitioning behavior obtained for Ti as a function of Na_2O_{melt} when compared to Sn, Zr and Hf (Table 7). As a consequence, $D_{Ti}^{cpx/melt}$ values of experiments with elevated Na_2O_{melt} cannot be considered in the lattice strain fits. The fitting parameters E and r_0 were fixed

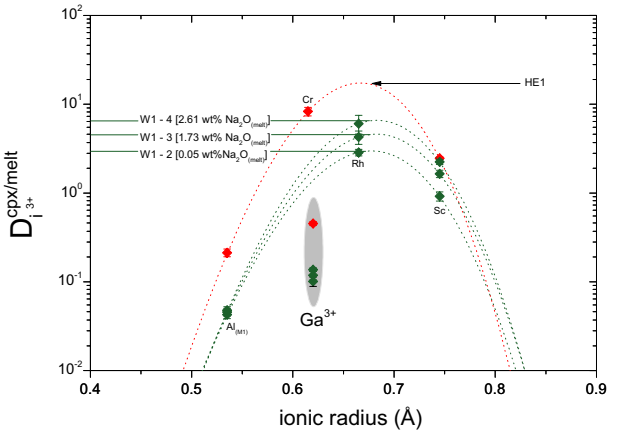

Fig. 10 Lattice strain parabolas of trivalent trace elements substituting into the M1 site of cpx displayed for the W1-2, W1-3 and W1-4 experiment, as well as for the HE1 experiment (combined partitioning data obtained in this study and in the study of Hill et al. (2000)). *Dotted lines* are emphasizing the weakness of the lattice strain fits, which are only based on three data points. However a general trend can be clearly taken from this approach, as both limps and the vertex of the parabola are defined. Ionic radii in [6]-fold coordination were taken from Shannon (1976). The values of the lattice strain parameters D_0, r_0 and E are displayed in Table 7. *Error bars* are one standard deviation

for all CMAS + xNa_2O experiments to the values obtained from the lattice strain fit of the sodium-free experiment (W1-2), as these values are not expected to change as a function of Na_2O_{melt} (see continuous lines in Fig. 11). It is worth pointing out that $D_{Ga}^{crystal/melt}$ is always offset to lower values when compared to what is predicted from the lattice strain fits (see Figs. 10, 12). This distinct behavior of $D_{Ga}^{cpx/melt}$ seems to be unrelated to the Na_2O_{melt} content, and was noticed in previous studies (Adam and Green 2006; Dygert et al. 2014), but not discussed in greater detail. To

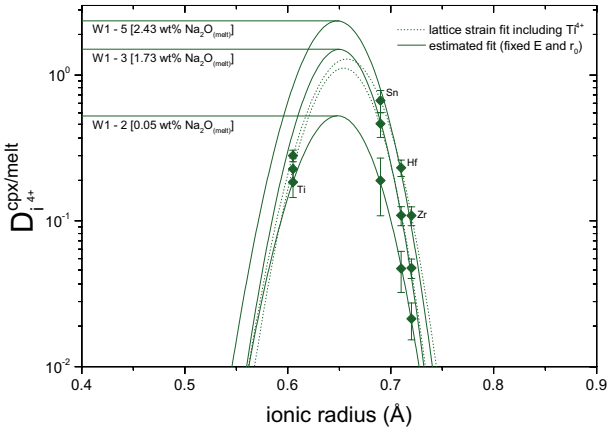

Fig. 11 Lattice strain parabolas of tetravalent trace elements substituting into the M1 site of cpx. E and r_0 obtained from the fitting cpx/melt partitioning data to the lattice strain function, were used as constants for the lattice strain fits of the sodium-bearing experiments. Ionic radii in [6]-fold coordination were taken from Shannon (1976). The values of the lattice strain parameters D_0, r_0 and E are displayed in Table 7. *Error bars* are one standard deviation

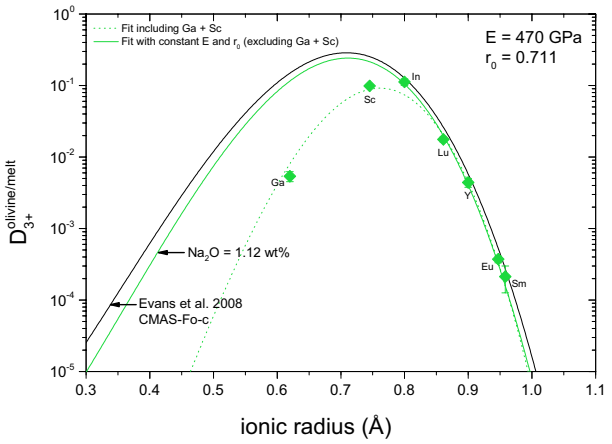

Fig. 12 Lattice strain model fit for the M1/2 site of olivine, determined using the partitioning data of the REE+Y and In. The value of $D_{Ga}^{\text{olivine/melt}}$ shows a distinct offset to the defined lattice strain parabola, in a similar way as found for the cpx M1 site. Lattice strain parameters of all experiments are displayed as a function of $Na_2O_{(melt)}$ (wt%). Ionic radii in [6]-fold coordination were taken from Shannon (1976). *Error bars* are one standard deviation. The values of the lattice strain parameters D_0, r_0 and E are displayed in Table 7. See text for details

explain this phenomenon, it could be assumed that Ga^{3+} enters the M2 site, or even the tetrahedral site of cpx, or that it is forming a specific melt complex with a major element, which still needs to be investigated in greater detail.

Olivine can be used to investigate if melt composition is influencing the crystal/silicate melt partitioning of trace elements, since its crystal chemistry is not affected by major element changes in the silicate glass. Fits of the $D_i^{\text{olivine/melt}}$ data to the lattice strain function (Blundy and Wood 1994) can reproduce results of $Na_2O_{(melt)}$-bearing experiments (Fig. 12). However, the lattice strain fit based on crystal/silicate melt partitioning of Ga, Sc, In and the REE + Y has to be evaluated in order to isolate crystal and melt compositional effects. First of all, when compared to relatively recent literature data (cf. Mallmann and O'Neill 2013; Evans et al. 2008) the obtained Young's modulus (E) of the lattice strain fit that includes Ga, Sc, in addition to the REE + Y partitioning data shows a distinct offset from previously reported values (≈200 GPa). The stiffness (high E value) of the olivine M1/M2 site in our experiments, is mainly controlled by the position of $D_{Ga}^{\text{olivine/melt}}$. Secondly, in previous partitioning studies, it was noticed that Sc substitution into olivine deviates from the mechanism of substitution of the REE (Evans et al. 2008). Taking this into account, we have excluded Ga and Sc partitioning data from the data that were used to obtain the lattice strain fitting parameters. In order to obtain valid lattice strain parameters, the REE + Y and In olivine/melt partitioning data of the Na_2O-free experiment (W1-2) was fitted to the lattice strain function (Eq. 5) using a fixed E-value derived from the experimental results of Evans et al. (2008), i.e., 470 GPa. The obtained value of r_0 of the Na_2O-free experiment can be used as a constant together with the E-value from the literature to derive values of D_0 for all experiments. The linear correlation of D_0 with Na_2O_{melt} obtained (Fig. 13) is in agreement with that observed for trivalent cations entering the M2 site of cpx (Fig. 9). This indicates that melt composition is more likely than crystal chemistry to be responsible for the observed changes in $D_{Ga}^{\text{olivine/melt}}$ as a function of Na_2O_{melt}.

Concluding remarks

Our results lead to the separation of crystal and melt compositional effects on trace element partitioning between clinopyroxene, olivine and silicate melt. Namely, increasing $^{[4]}Al$ into the cpx structure, while eliminating the effect of changes in degree of melt polymerization, will result in an increase of the $D_{\text{REE+Y}}^{cpx/melt}$, supporting previous findings (e.g., Lundstrom et al. 1994; Gaetani and Grove 1995; Lundstrom et al. 1998; Schosnig and Hoffer 1998; Blundy et al. 1998; Hill et al. 2000). By isolating crystal chemistry and melt structure effects, we show that cpx/silicate melt partitioning of Sn, Ba, In and Ga also increase as a function of $^{[4]}Al$, which was not accomplished in previous studies. There is still a need for further investigations to fully resolve the effect of Na_2O_{melt} on the crystal/silicate melt trace element partitioning. Our results indicate that Na may act to break "REE–Al

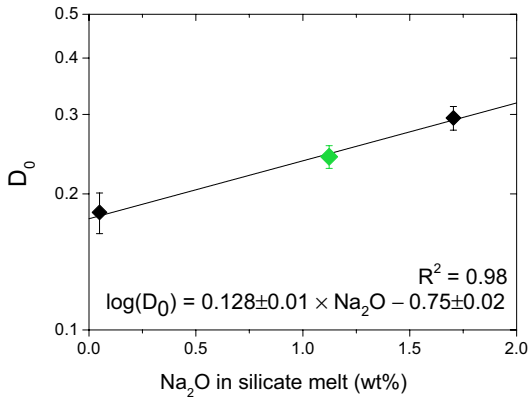

Fig. 13 Variations in D_0 for the M1/2 sites of olivine are displayed as a function of $Na_2O_{(melt)}$. The *symbol colored in light green* is the representative D_0 value of the lattice strain parabola depicted in Fig. 12

complexes" in the melt (e.g., Schosnig and Hoffer 1998), causing an increase in the activity coefficient of trace elements and consequently, $D_i^{crystal/melt}$. This becomes particularly important because most experimental datasets of crystal/silicate melt trace element partitioning dealt with simplified systems, with less than 0.5 wt% of Na_2O in the melt (e.g., Gaetani and Grove 1995; Hill et al. 2000; Mallmann and O'Neill 2009), while in natural samples, such as the mid-ocean ridge basalts, this element may be present in average concentrations of 2.8 wt% (Gale et al. 2013), but can be as high as 6 wt% (Jenner and O'Neill 2012). Moreover, it is important to consider all the parameters that may be affecting the observed $D_i^{crystal/melt}$ values, in order to have meaningful results when applying the lattice strain model theory (Blundy 1994), as exemplified, for instance, by the misfit of $D_{Ga,Ti,Al}^{crystal/melt}$.

Acknowledgements We are grateful to two anonymous reviewers for their comments, which greatly improved the manuscript, and to H. Keppler for his editorial handling. We thank N. Jung, T. Schulz, D. Lülsdorf and K. Brückel for their technical support at the University of Bonn. We are indebted to Chris Ballhaus for discussion, comments and suggestions. R.F. acknowledges financial support from the Deutsche Forschungsgemeinschaft (via DFG Grant FO 698/3). F.P.L. was supported by a PhD scholarship from DAAD/CNPq (Grant 248562/2013-4). This manuscript is contribution no. 39 of the LA-ICP-MS laboratory of the Steinmann Institute for Geosciences, University of Bonn.

References

Adam J, Green T (2006) Trace element partitioning between mica- and amphibole-bearing garnet lherzolite and hydrous basanitic melt: 1. Experimental results and the investigation of controls on partitioning behaviour. Contrib Mineral Petrol 152:1–17

Bennett SL, Blundy J, Elliott T (2004) The effect of sodium and titanium on crystal-melt partitioning of trace elements. Geochim Cosmochim Acta 68:2335–2347

Blundy J, Wood B (1994) Prediction of crystal-melt partition coefficients from elastic moduli. Nature 372:452–454

Blundy JD, Falloon TJ, Wood B, Dalton J (1995) Sodium partitioning between clinopyroxene and silicate melts. J Geophys Res 100:501–515

Blundy JD, Robinson JAC, Wood BJ (1998) Heavy REE are compatible in clinopyroxene on the spinel lherzolite solidus. Earth Planet Sci Lett 160:493–504

Blundy JD, Wood BJ (2003) Partitioning of trace elements between crystals and melts. Earth Planet Sci Lett 210:383–397

Chemia Z, Dolejs D, Steine-Neumann G (2015) Thermal effects of variable material properties and metamorphic reactions in a three component subducting slab. J Geophys Res B Solid Earth 1220:6823–6845

Davis FA, Humayun M, Hirschmann MM, Cooper RS (2013) Experimentally determined mineral/melt partitioning of first-row transition elements (FRTE) during partial melting of peridotite at 3 GPa. Geochim Cosmochim Acta 104:232–260

Duffy JA (1993) A review of optical basicity and its applications to oxidic systems. Geochim Cosmochim Acta 57:3961–3970

Dygert N, Liang Y, Hess P (2013) The importance of melt TiO_2 in affecting major and trace element partitioning between Fe-Ti oxides and lunar picritic glass melts. Geochim Cosmochim Acta 106:134–151

Dygert N, Liang Y, Sun C, Hess P (2014) An experimental study of trace element partitioning between augite and Fe-rich basalts. Geochim Cosmochim Acta 132:170–186

Ertel W, O'Neill HStC, Sylvester PJ, Dingwell, DB (2006) Solubilities of Pt and Rh in a haplobasaltic silicate melt at 1300ÂřC. Geochim Cosmochim Acta 63:2439–2449

Evans TM, O'Neill HStC, Tuff J (2008) The influence of melt composition on the partitioning of REEs, Y, Sc, Zr and Al between forsterite and melt in the system CMAS. Geochim Cosmochim Acta 72:5708–5721

Farges F, Brown GE Jr, Rehr JJ (1996) Coordination chemistry of Ti(IV) in silicate glasses and melts: I. *XAFS* study of titanium coordination in oxide model compounds. Geochim Cosmochim Acta 60:3023–3038

Flemming RL, Luth RW (2002) ^{29}Si MAS NMR study of diopside-Ca-Tschermak clinopyroxenes: detecting both tetrahedral and octahedral Al substitution. Am Mineral 87:25–36

Fonseca ROC, Mallmann G, Sprung P, Sommer JE, Heuser A, Speelmanns IM, Blanchard H (2014) Redox controls on tungsten and uranium crystal/silicate melt partitioning and implications for the U/W and Th/W ratio of the lunar mantle. Earth Planet Sci Lett 404:1–13

Gaetani GA (2004) The influence of melt structure on trace element partitioning near the peridotite solidus. Contrib Mineral Petrol 147:511–527

Gaetani GA, Grove TL (1995) Partitioning of rare earth elements between clinopyroxene and silicate melt: crystal-chemical controls. Geochim Cosmochim Acta 59:1951–1962

Gale A, Dalton CA, Langmuir CH, Schilling JG (2013) The mean composition of ocean ridge basalts. Geochem Geophys Geosyst 14:1–29

Hess PC (1991) The role of high field strength cations in silicate melts. In: Perchuk LL, Kushiro I (eds) Physical chemistry of magmas. Springer, New York, pp 152–191

Hill E, Wood BJ, Blundy JD (2000) The effect of Ca-Tschermaks component on trace element partitioning between clinopyroxene and silicate melt. Lithos 53:203–215

Huang F, Lundstrom CC, McDonough WF (2006) Effect of melt structure on trace-element partitioning between clinopyroxene and silicic, alkaline, aluminous melts. Am Mineral 91:1385–1400

Jarosewich E, Nelen J, Norberg JA (1980) Reference samples for electron microprobe analyses. Geostandard Newslett 4:43–47

Jenner FE, O'Neill HStC (2012) Analysis of 60 elements in 616 ocean floor basaltic glasses. Geochem Geophys Geosyst 13:1525–2027

Jochum KP, Weis U, Stoll B, Kuzmin D, Yang Q, Raczek I, Jacob DE, Stracke A, Birbaum K, Frick DA et al (2011) Determination of reference values for NIST SRM 610–617 glasses following ISO guidelines. Geostand Geoanal Res 35:397–429

Kohn SC, Schofield PF (1994) The importance of melt composition in controlling trace-element behaviour: an experimental study of Mn and Zn partitioning between forsterite and silicate melts. Chem Geol 117:73–87

Laurenz V, Fonseca ROC, Ballhaus C (2010) Solubility of palladium in picritic melts: 1. the effect of iron. Geochim Cosmochim Acta 74:2989–2998

Laurenz V, Fonseca ROC, Ballhaus C, Jochum KP, Heuser A, Sylvester PJ (2013) The solubility of palladium and ruthenium in picritic melts: 2. the effect of sulfur. Geochim Cosmochim Acta 108:172–183

Leitzke FP, Fonseca ROC, Michely LT, Sprung P, Münker C, Heuser A, Blanchard H (2016) The effect of titanium on the partitioning behavior of high-field strength elements between silicates, oxides and lunar basaltic melts with applications to the origin of mare basalts. Chem Geol 440:219–238

Longerich HP, Jackson SE, Günther D (1996) Inter-laboratory note. Laser ablation inductively coupled plasma mass spectrometric transient signal data acquisition and analyte concentration calculation. J Anal At Spectrom 11:899–904

Lundstrom CC, Shaw HF, Ryerson FJ, Phinney DL, Gill JB, Williams Q (1994) Compositional controls on the partitioning of U, Th, Ba, Pb, Sr and Zr between clinopyroxene and haplobasaltic melts: implications for uranium series disequilibria in basalts. Earth Planet Sci Lett 128:407–423

Lundstrom CC, Shaw HF, Ryerson FJ, Williams Q, Gill J (1998) Crystal chemical control of clinopyroxene-melt partitioning in the Di-Ab-An system: implications for elemental fractionations in the depleted mantle. Geochim Cosmochim Acta 62:2849–2862

Mallmann G, Fonseca ROC, Silva AB (2014) An experimental study of the partitioning of trace elements between rutile and silicate melt as a function of oxygen fugacity. An Acad Bras Cienc 86:1609–1629

Mallmann G, O'Neill HStC (2009) The crystal/melt partitioning of V during mantle melting as a function of oxygen fugacity compared with some other elements (Al, P, Ca, Sc, Ti, Cr, Fe, Ga, Y, Zr and Nb). J Petrol 50:1765–1794

Mallmann G, O'Neill HStC (2013) Calibration of an empirical thermometer and oxybarometer based on the partitioning of Sc, Y and V between olivine and silicate melt. J Petrol 54:933–949

Malvin DJ, Drake MJ (1987) Experimental determination of crystal/melt partitioning of Ga and Ge in the system forsterite-anorthite-diopside. Geochim Cosmochim Acta 51:2117–2128

Marquardt DW (1963) An algorithm for least-squares estimation of nonlinear parameters. J Soc Ind Appl Mech 11:431–441

Mills KC (1998) The influence of structure on the physico-chemical properties of slags. ISIJ Int 33:148–155

Mollo S, Blundy JD, Iezzi G, Scarlato P, Langone A (2013) The partitioning of trace elements between clinopyroxene and trachybasaltic melt during rapid cooling and crystal growth. Contrib Mineral Petrol 166:1633–1654

Moretti R (2005) Polymerisation, basicity, oxidation state and their role in ionic modelling of silicate melts. Ann Geophys Italy 48:583–608

Mysen BO (1990) Relationships between silicate melt structure and petrologic processes. Earth Sci Rev 27:281–365

Mysen BO (2004) Element partitioning between minerals and melt, melt composition, and melt structure. Chem Geol 213:1–16

O'Neill HStC, Berry AJ, Eggins SM (2008) The solubility and oxidation state of tungsten in silicate melts: implications for the comparative chemistry of W and Mo in planetary differentiation processes. Chem Geol 255:346–359

O'Neill HStC, Eggins SM (2002) The effect of melt composition on trace element partitioning: an experimental investigation of the activity coefficients of FeO, NiO, CoO, MoO_2 and MoO_3 in silicate melts. Chem Geol 186:151–181

O'Neill HStC, Palme H (1998) Composition of the silicate Earth: implications for accretion and core formation. In: Jackson I (ed) The Earth's mantle: structure, composition and evolution. Cambridge University Press, Cambridge, pp 3–126

Onuma N, Higuchi H, Wakita H, Nagasawa H (1968) Trace element partitioning between two pyroxenes and the host lava. Earth Planet Sci Lett 5:47–51

Ponader CW, Brown GE (1998) Rare earth elements in silicate glass-melt systems: I. Effects of composition on the coordination environments of La, Gd, and Yb. Geochim Cosmochim Acta 53:2893–2903

Prowatke S, Klemme S (2005) Effect of melt composition on the partitioning of trace elements between titanite and silicate melt. Geochim Cosmochim Acta 69:695–709

Ryerson FJ, Hess PC (1978) Implication of liquid-liquid distribution coefficients to mineral-liquid partitioning. Geochim Cosmochim Acta 42:921–932

Schosnig M, Hoffer E (1998) Compositional dependence of REE partitioning between diopside and melt at 1 atmosphere. Contrib Mineral Petrol 133:205–216

Shannon RD (1976) Revised effective ionic radii and systematic studies of interatomie distances in halides and chaleogenides. Acta Crystallogr A 32:751–767

Westrenen WV, Allan NL, Blundy JD, Purton JA, Wood BJ (2000) Atomistic simulation of trace element incorporation into garnets—comparison with experimental garnet-melt partitioning data. Geochim Cosmochim Acta 64:1629–1639

Westrenen WV, Wood BJ, Blundy JD (2001) A predictive thermodynamic model of garnet-melt trace element partitioning. Contrib Mineral Petrol 142:219–234

Wood BJ, Blundy JD (1997) A predictive model for rare earth element partitioning between clinopyroxene and anhydrous silicate melt. Contrib Mineral Petrol 129:166–181